KHLEUVEN

KATHOLIEKE HOGESCHOOL LEUVEN

ACADEMIC YEAR 2013-2014

DEVELOPMENT OF CNT GROWTH RECIPES ON NI/TIN BLANKETS

Waldo Vandermeiren

Chemistry

Thesis submitted to obtain the degree of professional bachelor in chemistry
Promotor: Dr. T. Mortier, KHLeuven, G&T
Internship at: IMEC, ECAT group
Supervisor: M. van der Veen

Acknowledgements

Above all, I would like to thank Marleen van der Veen for giving me the chance to work on this project, for the support during my internship and for giving me the opportunity to glance at R&D and the world around it. I would also like to thank Tom Mortier to rekindle the passion for nanotechnology, through the motivating and entertaining classes, and for the support during this internship. In addition, I would like to thank Chiara Alessandri for the support during the writing of this thesis. Lastly, I would like to thank imec, as a whole, for the use of their infrastructure and the overall experience.

Abstract

An experimental study of carbon nanotube growth (CNT) has been performed using plasma enhanced chemical vapor deposition with acetylene (C_2H_2) as a hydrocarbon precursor and nickel (Ni) as the catalyst on a titanium nitride (TiN) substrate. The experimental results have been compared to the earlier work of Nicolò Chiodarelli performed on the same tool. A comparative study has been conducted between different pretreatment recipes, including: NH_3 plasma, H_2 plasma, thermal and no catalyst pretreatment at different set temperatures, ranging from 800-500°C. In addition, the influence of total and partial pressure has been investigated at a constant set temperature. This latter experiment shows signs of a total pressure optimum at a constant partial pressure. Although, more research needs to be conducted to confirm this finding.

Table of contents

Glossary

BSE	Backscattered secondary electrons
CL	Cathodoluminescence
CMOS	Complementary metal oxide semiconductor
CNF, CNFs	Carbon nanofiber(s)
CNT, CNTs	Carbon nanotube(s)
CVD	Chemical vapor deposition
DWCNT, DWCNTs	Double walled carbon nanotube(s)
EBSD	Diffracted backscattered electrons
eV	Electron Volt ($1.6 * 10^{-19}$ J)
FEG	Field emission gun
HRTEM	High resolution transmission electron microscope
MHz	Megahertz (10^6 Hz)
mm	Millimeter (10^{-3} m)
mT	Millitorr (10^{-3} T)
MWCNT, MWCNTs	Multi walled carbon nanotube(s)
nm	Nanometer (10^{-9} m)
PECVD	Plasma enhanced chemical vapor deposition
RF	Radio frequency
sccm	Standard cubic centimeters per minute (cm^3/min)
SCCNF, SCCNFs	Stacked cone carbon nanofiber(s)

SEM	Scanning electron microscope
SE	Secondary electrons
SWCNT, SWCNTs	Single walled carbon nanotube(s)
T	Torr
TEM	Transmission electron microscope
μm	Micrometer (10^{-6} m)
VLS	Vapor-liquid-solid

1. Introduction

The story of carbon nanotubes (CNTs) started in 1952 with the first report by L.V. Radushkevich and V.M. Lukyanovich. Since then many other research teams have made their contribution to the story without initiating much interest to the subject. It was only when S. Lijima experimented with the arc evaporation method, developed by D. Huffman and W. Kratschmer for producing microscopic amounts of C_{60}, that the interest boomed. He found that under certain conditions not only C_{60} was formed, but also tubular carbon structures, now known as multi walled carbon nanotubes (MWCNT). Simultaneously other groups made similar discoveries, which feeds the discussion on whom owes the 'discovery' of CNTs. Soon CNTs became a real hype, which has led to the uncovering of its extraordinary properties in the fields of mechanical strength, electrical and thermal conductivity and stability and optical properties. In the wake of these discoveries, many optimistic statements were made, viz:

- CNTs are a 100 times stronger than stainless steel and six times lighter;
- CNTs are as hard as diamond with a thermal capacity which is twice that of pure diamond;
- CNTs current-carrying capacity is 1000 times higher than that of copper;
- CNTs are thermally stable up to 4000K;
- CNTs can be metallic or semiconducting, depending on their diameter and chirality.

Even though these properties only apply to atomically perfect CNTs, which are far from the ones that are practically produced today, they made people dream about future applications. One of the most ambitious dreams is NASA's space elevator, in which the cable would consist of CNTs. (Figure 1.1).

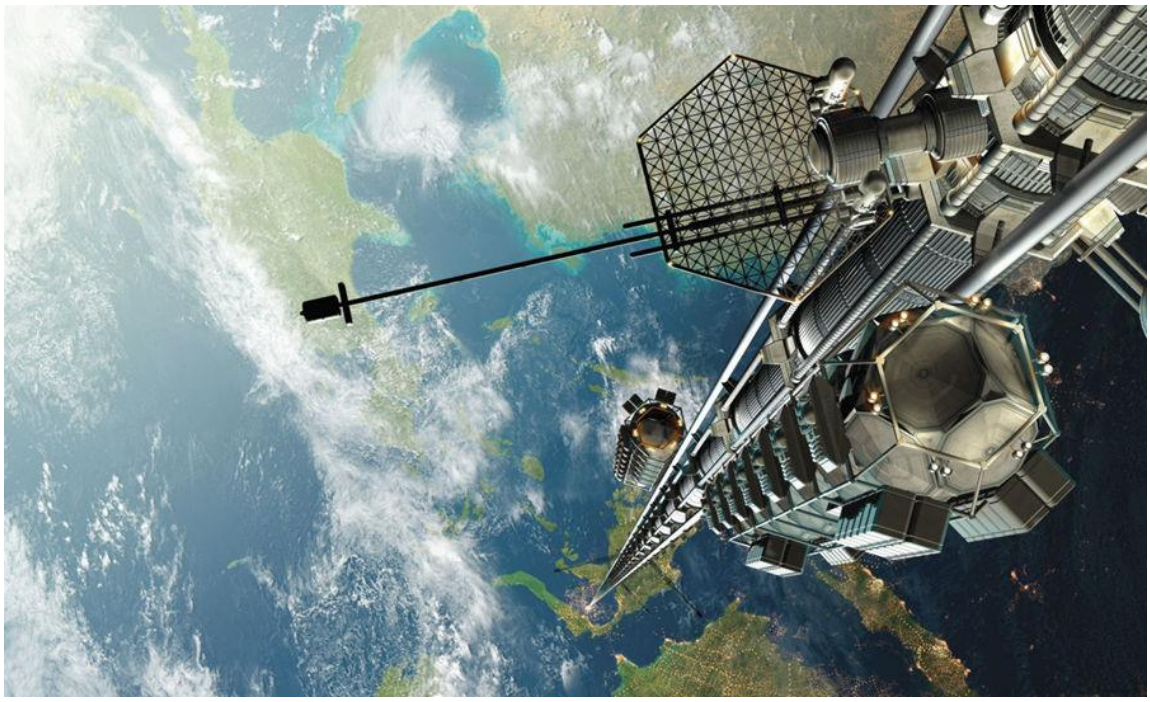

Figure 1.1: 3D model of a space elevator, an ambitious CNT-based project. [1]

Among other industries, CNTs have especially a lot to offer in microelectronics. As technology moves forward and chips become smaller, some commonly used materials are driven to their limits. One area in which CNTs can prove themselves is interconnects. Today's interconnects, made of copper, are having trouble maintaining their properties at sub 10 nm dimensions. At these dimensions, the resistivity and the produced heat are sufficiently high for the copper to melt at the desired current density. In addition, filling the interconnect vias is becoming increasingly difficult. CNT growth, as a bottom-up process, could provide a filling solution. However, high-yield CNT growth on conductive substrates remains challenging. Despite the fact that CNT shells feature ballistic transport of electrons over a larger distance (longer mean free path), whereas that of copper suffers from surface scattering, the overall conductivity of CNT interconnects has yet to match those of the copper ones due to several factors, i.e. CNT density, crystallinity, chirality, substrate-CNT-copper contacts, etc... In other words, there is still a lot of research to be done before implementation could become a reality. [2][3][4][5][6]

This thesis will give an introduction to CNTs and the production and analysis methods used for the experimental part. In addition, some theory will be presented concerning the growth mechanism and the analysis technique. The last chapters will cover the experimental work, which discusses catalyzed CNT growth with Ni on TiN. More specifically, it compares different pretreatment types and the influence of the total and partial pressures on quality and quantity of the growth.

1.1. What are carbon nanotubes?

1.1.1. General structure

Carbon nanotubes are quasi one-dimensional nanostructures and one of the many carbon allotropes that are categorized under fullerenes. The structure can be seen as a sheet of graphene wrapped into a cylindrical form. CNTs, like graphene, consist of sp^2 hybridized carbon atoms in a honeycomb lattice. One end of a tube is often closed due to formation of a buckyball-like hemisphere. Two main variants can be distinguished, single- and multi-walled carbon nanotubes (SWCNT and MWCNT). A SWCNT contains only one cylindrical shell, whereas an MWCNT contains multiple shells with different diameter, which are concentrically wrapped around each other. Like in graphite, these shells are kept together by Van der Waals forces with an inter-distance of 0.34 nm between shells. The difference between these two variants is shown in Figure 1.2. [12][13]

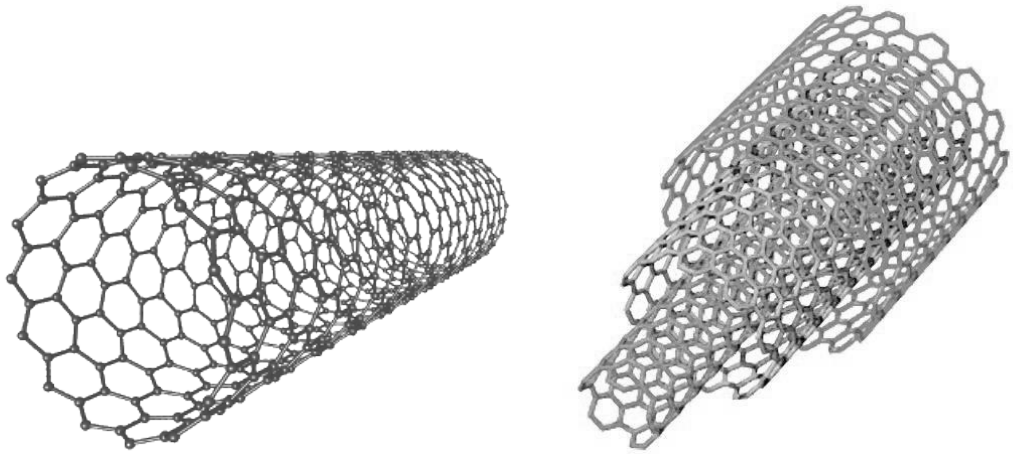

Figure 1.2: Model of a SWCNT (left) and a MWCNT (right). [7][8]

1.1.2. Architectural types & chirality

It is possible to differentiate three main architectural types: armchair (Figure 1.3a), zigzag (Figure 1.3b) and chiral (Figure 1.3c). Their names derive from the graphene sheets of which they consist. The architectural difference between these types is shown in Figure 1.3.

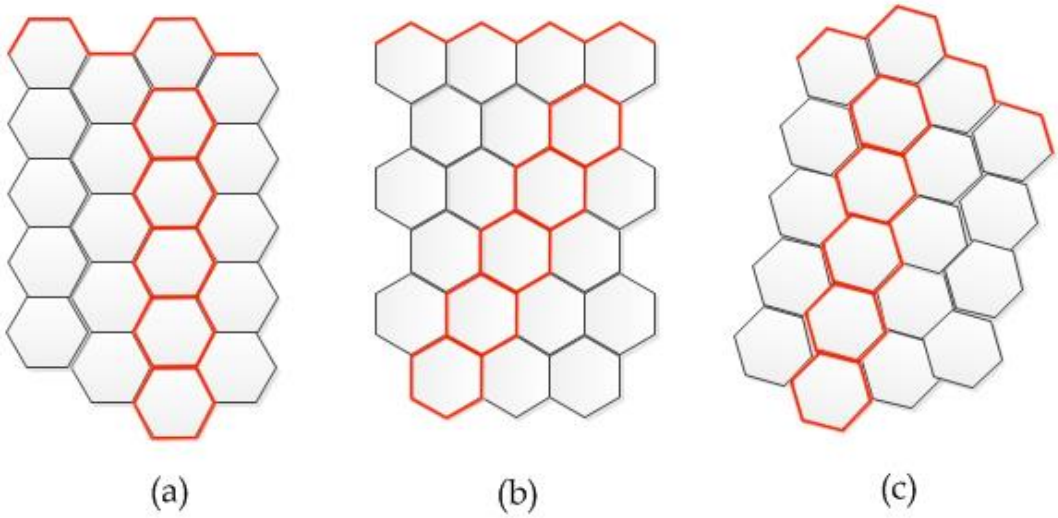

Figure 1.3: Structural architecture of the armchair type (a), zigzag type (b) and chiral type (c). [9]

The graphene sheet is described by two lattice translation vectors a_1 and a_2. In general, a CNT is described by the diameter and the helicity, also known

as the chirality. The chirality is determined by the chiral vector C_h, defined as:

$$C_h = n\,a_1 + m\,a_2,$$

with *n* and *m* as integer values, which are often displayed as *(n,m)*. Figure 1.4 shows how the chirality of a CNT can be determined. The blue lines represent the tube axis that, if joined together, would be the seam of the tube. Any point on the blue lines represents a carbon atom (point A). Subsequently, two lines need to be drawn on the lattice to find the chiral vector C_h. Firstly, the armchair vector is drawn in such a way that it separates the hexagons in the lattice into two equal halves(bottom dashed line in Figure 1.4). The carbon atom on one of the blue tube axis closest to this armchair line represents point B. Connecting point A and B gives the chiral vector C_h. Secondly, the zigzag line is drawn starting from point A and horizontally to the lattice. The angle formed between the chiral vector and the armchair, or zigzag, line determines the chirality. The integers n and m represent this angle, which are n=5 and m=2 in the example given in Figure 1.4.

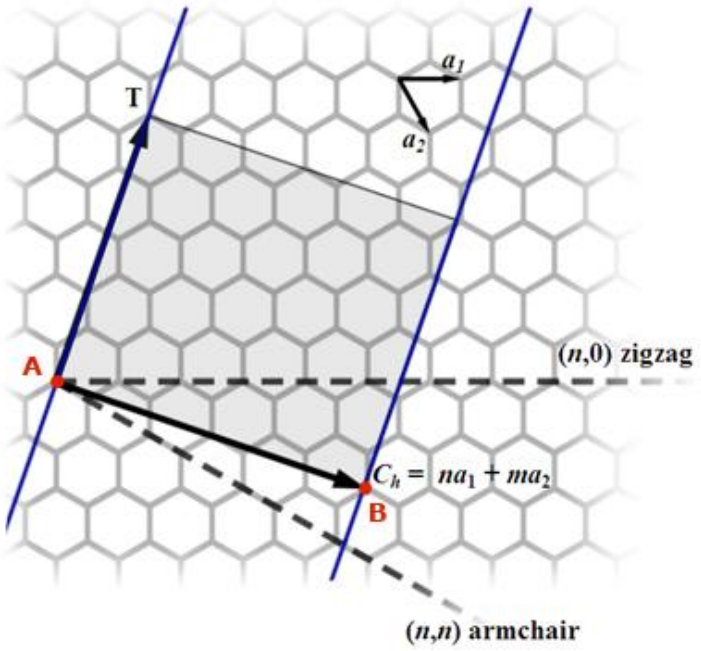

Figure 1.4: Illustration for determining the chirality. [10]

When the angle Θ between the chiral vector and the armchair line is Θ = 0º, the tube is of the armchair type (n=m). When the angle is Θ = 30º, it represents the zigzag type. Everything in between belongs to the chiral type.

Armchair type CNTs are metallic at room temperature together with all CNTs that comply to the rule $n - m = 3p$ $(p = 1, 2, 3, \ldots)$. The example given in Figure 1.4 represents a metallic CNT (5-2=3). In other words, when the difference between n and m is a plurality of three, the nanotube behaves like a metal. All other CNTs meet either $n - m = 3p + 1$ or $n - m = 3p + 2$ $(p = 0, 1, 2, 3, \ldots)$ and are semiconductors. Here, the bandgap is inversely proportional to the tube diameter and can vary from zero to about 2 eV. An overview of the conductivity in relation to the chirality is shown in Figure 1.5.

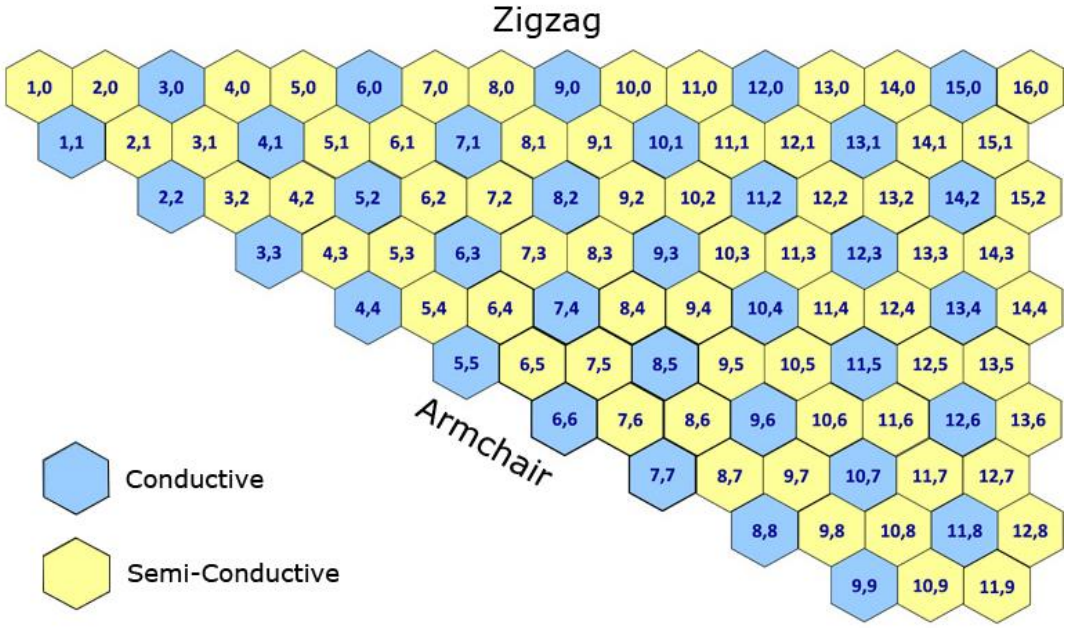

Figure 1.5: Overview of conductivity in relation to chirality. [11]

Theoretically, the diameter of the SWCNT can be described by the following equation:

$$d = \frac{\sqrt{3} * b}{\pi} \sqrt{(n^2 + nm + m^2)},$$

where *b* is the C-C bond length, set to be 0.142 nm. The term '$\sqrt{3} * b$' is often renamed to '*a'*, which is the lattice constant of the graphene structure.

In the case of MWCNTs there seems to be a correlation between the diameter and the number of shells. The following empirical equations are derived from experimental data.

$$\text{Literature data: } N_{Shells} \approx d_{CNT} - 1, \text{ with } \sigma_N \approx 0.23 * d_{CNT}$$

$$\text{Imec data: } N_{Shells} \approx 1.15 d_{CNT} - 2.5, \text{ with } \sigma_N \approx 0.21 * d_{CNT}$$

$$\text{Combined data: } N_{Shells} \approx d_{CNT} - 2, \text{ with } \sigma_N \approx 0.17 * d_{CNT}$$

These relations were obtained by plotting the average N_{Shells} of groups of 10 CNTs to their corresponding average diameter. [12][14][15][16][17]

1.1.3. Carbon nanofibers

Besides CNTs, other structures can be formed during the synthesis. One of them are carbon nanofibers (CNFs). In the case of CNTs the graphitic basal planes are oriented parallel to the fiber axis with a central hollow region (shell structure). In the case of CNFs, multiple types can be distinguished. When the graphitic basal planes are shaped like stacked cone segments, they are called 'Stacked Cup Carbon Nanofibers' or SCCNFs (stacked-cone structure, see Figure 1.6). This type retains the central hollow region and when this is lost, the stacked segments are called a 'fishbone'. However, when the graphitic basal planes are oriented perpendicularly to the fiber axis, they are called stacked CNFs (platelet structure). In this type, the central hollow region is lost. Two more variants are based on the stacked CNF model. In one of them the fibrils are coiled (platelet spiral structure). The second consists of a ribbon structure in which the planes are oriented parallel to the fiber axis (sometimes also referred to as carbon nanosheets).

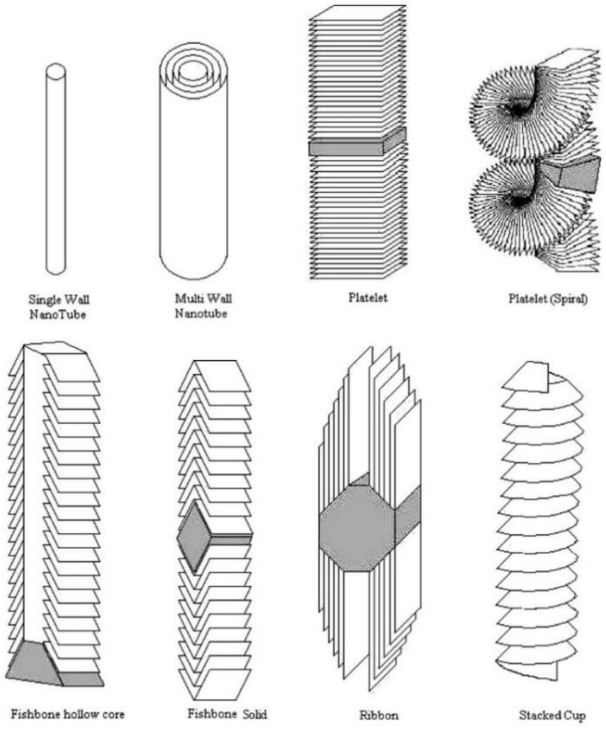

Figure 1.6: Overview of all main CNT and CNF types. [20]

In general, the difference between CNTs and CNFs can be noted by looking at the width, using a Scanning Electron Microscope (SEM). CNTs typically range from 1 to 30 nm, whereas CNFs range from 50 to 200 nm in width. Though tedious, the best structural characterization can be obtained using TEM analysis. Only in this way, the tubular structure can be visualized as shown in Figure 1.7. [12][20][21][22][23]

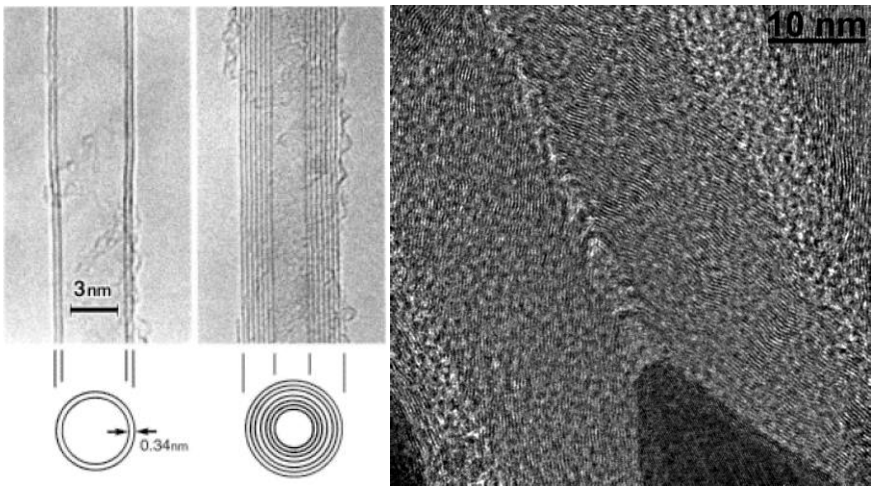

Figure 1.7: TEM imagery of a DWCNT and MWCNT (left) and a herringbone CNF (right). [18][19]

2. Growth mechanism

2.1. General mechanism

To this date, the growth mechanism of CNTs is not fully understood and still subject to debate. In this thesis, the most commonly accepted mechanism will be put forth, supplemented with recent findings. The mechanism can be divided into several parts that are adsorption, decomposition, diffusion and crystallization. Figure 2.1 shows an overview of the global mechanism.

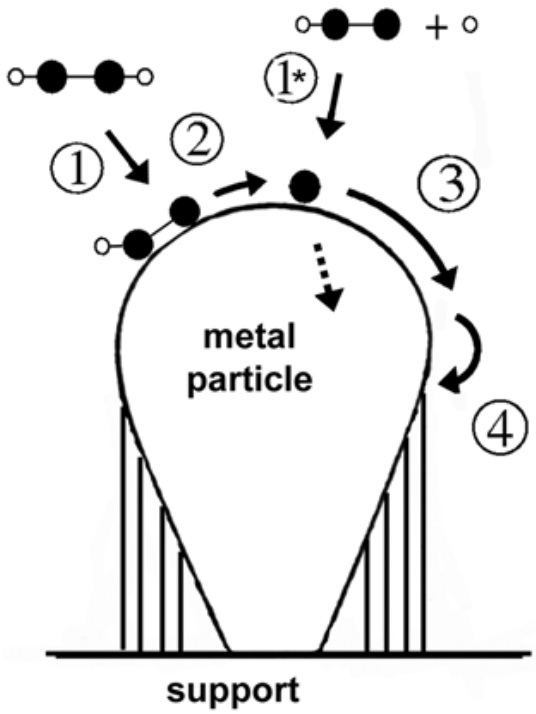

Figure 2.1: General CNT growth mechanism with 1) Adsorption, 1*) and 2) Decomposition, 3) Diffusion and 4) Crystallization. [19]

2.1.1. Adsorption

Once the carbon precursor (carbonaceous gas) is introduced, adsorption to the metal particle surface can occur.

2.1.2. Decomposition

The adsorption is followed by the decomposition of the precursor. It is well known that hydrocarbons are easily broken up by thermal decomposition (pyrolysis) at high temperatures. However when a suitable metal catalyst is introduced, decomposition can take place at lower temperatures (catalytic pyrolysis). The goal is to avoid aerial pyrolysis and their related by-products by proper selection of the precursor and catalyst. When catalytic pyrolysis takes place hydrogen is released from the particle surface while carbon stays adsorbed. In this process carbides are formed as intermediates in the reaction. The reaction equation for methane is shown below:

$$CH_4\,(g) + nM\,(s) \leftrightarrow M_nC\,(s) + 2H_2\,(g)$$

$$M_nC\,(s) \leftrightarrow nM\,(s) + C\,(s)$$

$$CH_4\,(g) \leftrightarrow C\,(s) + 2H_2\,(g)$$

The sequence of steps are as follows. Configuration A in Figure 2.2 represents acetylene as the starting point. Two decomposition paths can be considered: the first intermediate structure is shown as B1, in which a hydrogen atom is disconnected from the original structure; the second intermediate (B2) breaks down the C-C bond resulting in two C-H components. In theory, configuration B1 should be more common in the first stage of the decomposition due to the lower energy barrier. However, since the total energy of configuration B2 is much lower compared to the one of configuration B1, both are experimentally observed. The further course of the decomposition is shared by both intermediates.

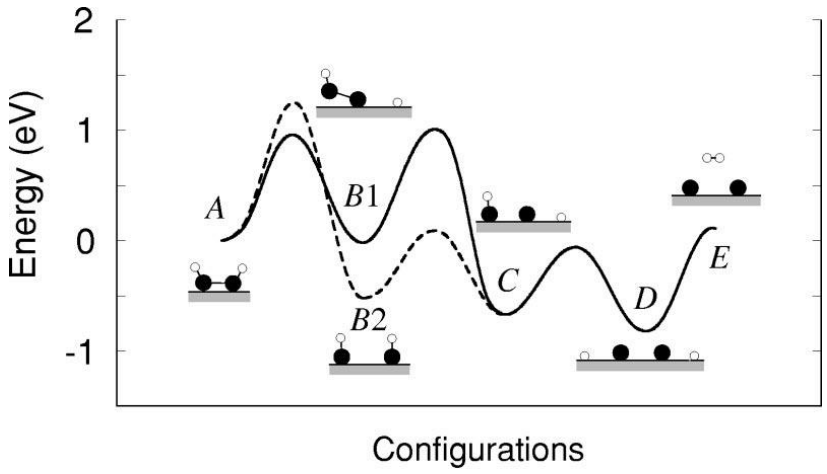

Figure 2.2: An overview of possible decomposition paths with their corresponding energy barrier. [24]

Next, the formation of H-H and C-C bonds take place. The type of the structure is partially dependent on the growth rate, which in turn depends on the surrounding gasses, temperature, etc... It is believed that when the formation rate of pentagonal and heptagonal rings is higher than their repair into hexagonal rings, than the resulting CNTs will be spiral or helical instead of straight (see §2.1.4 Crystallization). Finally, some hydrogen diffuses into the hollow part of the nanotube.

The formation of the decomposed carbon greatly depends on the precursor that is being used. It is believed that plasma can support the decomposition step by decreasing the mean free path of molecules and that it can enhance the dissolution and diffusion by locally heating the surface. [4][20]

2.1.3. Diffusion

Most of the CNT growth mechanistic studies seem to debate this step.

Bulk diffusion

This commonly accepted mechanism was proposed by Baker et al. in the early 1970's. The bulk diffusion mechanism originates from the Vapor-Liquid-Solid (VLS) mechanism, which implies that the catalyst forms a liquid droplet. After the decomposition step, the adsorbed carbon on top is dissolved into the particle. The dissolved carbon diffuses through the particle.

When a state of supersaturation is reached within the particle, the carbon will precipitate at the bottom end to form the body of the carbon filament. Due to the exothermic nature of the decomposition of hydrocarbons, and the endothermic nature of the crystallization process, it is believed that a temperature gradient exists across the particle. Because the solubility of carbon in a metal is temperature dependent, precipitation of excess carbon will take place at the colder bottom part of the particle (crystallization site). At the same time a concentration gradient is established within the particle, which keeps the diffusion process going. The combination of these two gradients is essential for the growth process. Carbon diffusion in general is believed to be the rate-limiting step in the growth process. Although this is true in most cases, under the same conditions (using acetylene), the carbon diffusion rate in metallic Fe is two to three orders of magnitude larger than for Ni or Co, even though the growth rate for Ni and Co is higher. When the top of the catalyst is poisoned, the growth rate is reduced. A common cause of catalyst poisoning is the formation of a graphitic cap covering the particle surface (closing of the tube), which prevents the precursor from reaching the catalyst site. It should be noted that during the decomposition and the dissolution carbides are formed. The stability of these carbides is dependent on the carbon coverage. When the state of supersaturation is reached, all carbides are disintegrated. The process of bulk diffusion is shown in Figure 2.3.

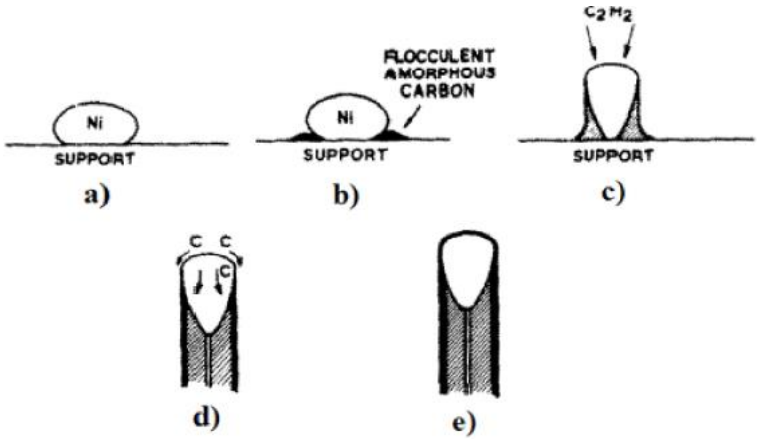

Figure 2.3: The process of bulk diffusion. [25]

This model contains some irregularities though. First of all, the phase of the catalyst is uncertain. CNF and CNT growth has been reported at temperatures lower than 300°C and 600°C respectively. This is well below the size-corrected metal-carbon eutectic temperature, which implies that the catalyst can be solid in contrast to VLS. In addition, Moisala et al. found that the melting point of several transition metals only changes for particles smaller than 10 nm, and in order to be liquid they would have to be smaller than 3 nm. Secondly, not all hydrocarbon decompositions are exothermic (e.g. CH_4) and yet they yield CNT growth. Thirdly, the model does not account for small particles. Because metals have a high thermal conductivity, the heat released during the exothermic decomposition would most likely heat up the entire particle, leaving the concentration gradient as the main driving force for the carbon diffusion across the metal particle. Therefore Barid et al. proposed a secondary diffusion mechanism known as the surface diffusion. [26][27]

Surface diffusion

This model suggests that metal-hydrocarbon species move over the particle surface and dissociate at a contact angle between the particle and the substrate. Thereby a carbon layer is formed which follows the surface of the particle and exerts a force strong enough to lift up the particle from the substrate. This action results in the forming of a filament alongside the particle. The filament is kept hollow because no carbon supply can reach the bottom of the particle. The diffusion and therefore the growth continues until the metal supply at the top of the particle is insufficient or when the top of the particle is covered with a graphitic layer (closing of the tube). Figure 2.4 shows the process of surface diffusion.

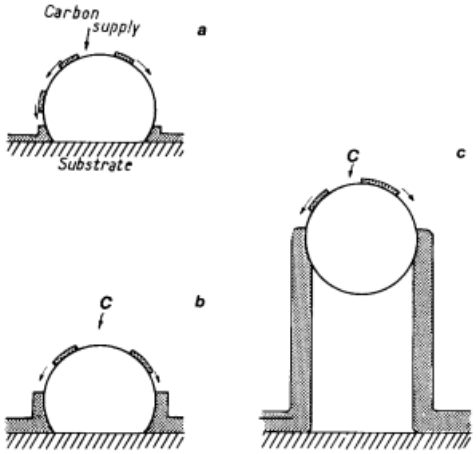

Figure 2.4: The process of surface diffusion. [12]

The question still remains whether one mechanism is more plausible than the other or if both mechanisms compete in some way. The answer may lie in the middle. It may be that surface and subsurface diffusions are favored at lower growth temperature, while bulk diffusion occurs at higher temperatures. This idea originates from the fact that the energy barrier for (sub)surface diffusion is lower than the one for bulk diffusion (see *Subsurface diffusion* for energy barrier values on Ni). Both surface and bulk diffusion have been directly observed. It should be noted that these observations were made by in situ HRTEM, which do not entirely represent CVD conditions in terms of gas flow, pressure, temperature, substrate specimen, etc.... The diffusion mechanism that occurs is highly dependent on temperature, the type of metal catalyst and the carbon precursor used. [6][12][20][27][28]

Subsurface diffusion

A third form of diffusion can occur in which the carbon travels 1-2 layers below the surface of the metal particle. By studying the surface diffusion on different Ni crystalline structures, Hofmann et al. found that carbon atoms diffuse on the surface of the closely packed Ni(111) surface, while subsurface diffusion is favored on the energetically less favored Ni(100) surface, where the atom corrugation is much deeper. In comparison, carbon on a Ni(111) surface bonds with 3 Ni atoms, or 2 in a transition state, while on a Ni(100) it bonds with 5 Ni atoms, further away, which makes diffusion harder. As a

result, the energy barrier for surface diffusion on Ni(111) is 0.4 eV, while for Ni(100) it is 1.9 eV.

In the case of Ni(100) there are two main reasons to believe that subsurface diffusion is favored over surface and bulk diffusion. First, the benefit of subsurface diffusion compared to surface diffusion is that, although more Ni-C bonds exist, less bonds have to be broken at the same time. Second, carbon is incorporated into an octahedral interstitial site in the Ni lattice, which requires a volume expansion. This makes the subsurface an optimum site. While a volume expansion in the bulk is quite hard, in the subsurface some relaxation is allowed by pushing up the surface layer. The energy barrier calculations support this hypothesis. The barrier for surface diffusion on Ni(100) is found to be 1.9 eV, bulk diffusion ~1.6 eV and subsurface diffusion ~1.0 eV. Although subsurface diffusion has not yet been measured for every crystal structure, it is believed to be a general diffusion mechanism that can be applied to metal structure. [27][29][30]

2.1.4. Crystallization

The crystallization step starts at the point of supersaturation as mentioned in the above. The carbon shells are hereby formed on the step edge of the metal particle as shown below in Figure 2.5.

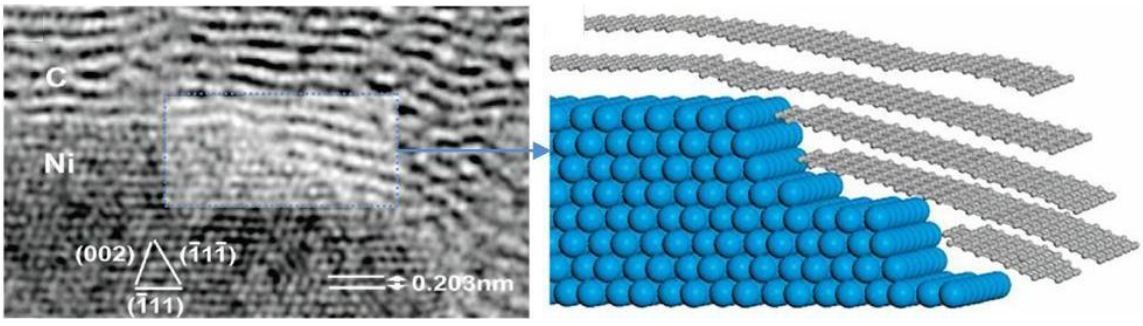

Figure 2.5: Crystallization of carbon on the step edge of the catalyst particle, TEM image (left), 3D model (right). [6]

As mentioned before, the growth rate plays a major role in the creation of the shells. It is believed that at high growth rates the formation of pentagonal and heptagonal rings is favored over the one of the hexagonal

ring. This leads to curly CNTs. The structure is still able to repair itself to some extent if the growth rate does not transcend the repair rate. At low growth rates, however, only the hexagonal rings are formed, so the structure quality is improved. [19][20]

2.2. Ostwald ripening effect

Ostwald ripening is a spontaneous process in which large particles grow even larger at the expense of smaller particles surrounding them. This phenomenon is driven by the reduction of surface free energy. Molecules on the surface of the particles are energetically less stable than those in the bulk, which are stabilized by the surrounding molecules in every direction. A second mainspring is the overall energy state of the particle. Smaller particles have a higher surface area to volume ratio, which corresponds to a higher overall energy state. Therefore, surface molecules often leave the surface of smaller particles and redeposit onto the surface of larger particles when supersaturation is reached. So, although small particles are kinetically favored, large particles are thermodynamically favored. This process is shown below in Figure 2.6.

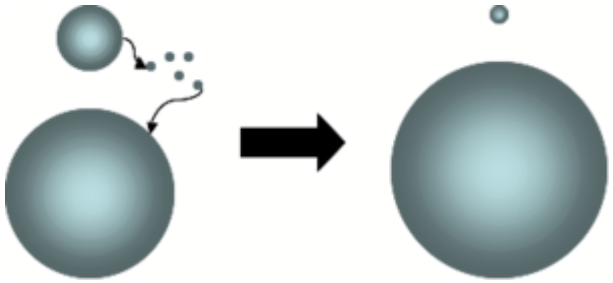

Figure 2.6: A visual representation of the Ostwald ripening effect. [31]

When a catalyst film is subjected to annealing, the film will break up into particles. Since the temperature increases, the mobility of the catalyst atoms increases as well, therefore Ostwald ripening can occur. Catalysts with a high inward diffusion rate and porosity are generally believed to have low Ostwald ripening rates. Because Ostwald ripening can alter the catalytic activity and

size, the choice of the catalyst influences the outcome to some extent. [12][32][33]

2.3. Why nickel as a catalyst?

The metal type plays a vital role in the carbon decomposition and diffusion step. Transition metals like Fe, Co and Ni are favored because of their ability to overlap empty d-shells with hydrocarbon bonds and therefore facilitate the decomposition (catalysis). When it comes to the diffusion step, the solubility of carbon in these metals is relatively high compared to other transition metals. The highest solubility occurs for those metals that form carbides. The carbide intermediate should not be too stable in order to form the end product. In addition, they cause a high diffusion rate. At last, they have a better adhesion to the carbon lattice, which allows the formation of smaller tubes due to a stronger curvature. [19][30]

2.4. Why titanium nitride as a substrate?

Given the future application for these nanotubes, the main requirement for the substrate is to be conductive. Although, this has as a consequence that the grown nanotubes will be predominantly MWCNTs. In addition, TiN forms a protective barrier layer against diffusion of the Ni catalyst, which prevents the catalyst from falling through the substrate at small dimensions. Last, the TiN layer prevents the formation of $NiSi_x$. Without the barrier layer silicide formation would occur at temperatures above 300°C. [34][35]

2.5. Tip vs Base growth

Two models of CNT growth can be distinguished depending on the catalyst-substrate interaction. When the catalyst substrate interaction is weak, the

catalyst will have a convex shape. This results in a limited contact area. In this case the carbon will precipitate out across the metal bottom, i.e. the area between the metal and substrate, as can be seen in Figure 2.7(i). The deposition of carbon at the bottom exerts a force great enough to lift the particle of the substrate and move it upwards (ii). The growth continues as long as the precursor can reach the particle top. Once the particle top is encapsulated, the growth process will come to an end (iii). This is known as the tip-growth model.

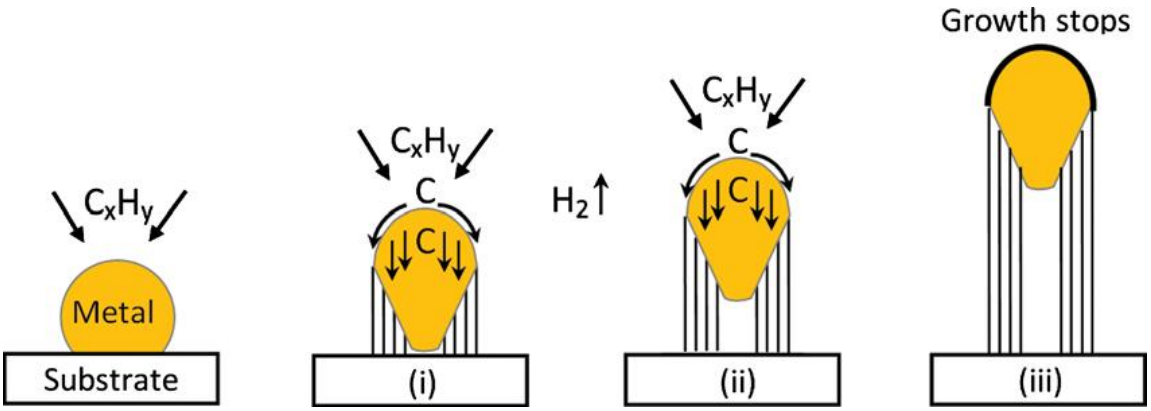

Figure 2.7: Visual representation of the tip-growth mechanism. [4]

On the other hand, when the catalyst-substrate interaction is strong, the catalyst droplet takes on a more flat form (a lower contact angle), in which there is no free space left between the particle and the substrate for carbon to precipitate .In this case, the carbon is forced to emerge out from the particle's apex to form a crystallized hemispherical cap over the particle surface. This cap then extends further upwards in the form of a seamless cylinder. The precursor is decomposed on the lower part of the particle surface, not taken by the cap. This way the carbon diffuses upwards and the CNT grows up with the catalyst rooted on its base. Hence, this is known as the base-growth model. A visual representation of the mechanism is shown below in Figure 2.8.

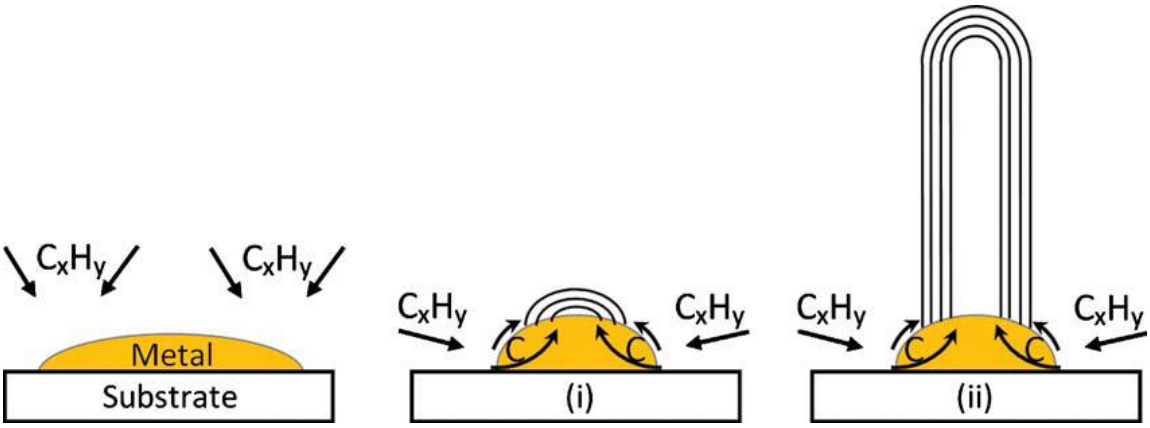

Figure 2.8: Visual representation of the base-growth mechanism. [4]

In general, it can be said that tip-growth mainly occurs on metallic surfaces, while base-growth occurs on oxide surfaces. Although, there is evidence to believe that the growth mode is dependent on different parameters. It has been reported by Gohier et al. that the growth mode can change from tip- to base-growth with decreasing particle size using the same conditions (catalyst, substrate, etc…). However, these experiments have only been performed on an oxide substrate (SiO_2). In addition Song et al. reported that catalysts which are partially interconnected prefer base-growth, while isolated particles favor tip-growth. Delzeit et al. showed that an increase in plasma power results in a transition from MWCNTs to nanofibers, which show tip- and base-growth respectively. Song et al. also showed that variation in plasma power can alter the growth mode. To conclude, it is clear that more parameters play a role in determining the growth mode than catalyst-support adhesion alone. [4][19][36][37][38]

3. Synthesis

3.1. Chemical Vapor Deposition

In general, chemical vapor deposition (CVD) is a widely used technique to process materials. The majority of its applications involve applying solid thin-film coatings to surfaces using a wide range of materials. In addition, it is used to produce bulk materials, powders, composites and nanomaterials. In the case of CNT growth, the CVD technique is used as follows. A carbonaceous precursor passes through a heated reaction chamber in which a catalyst material is present. The chamber is heated to sufficiently high temperatures at which the catalyst is able to decompose the precursor (typically between 600-1200°C). The precursor can be supplied to the chamber in any phase. In case liquid hydrocarbons are used, the liquid is preheated before being purged by an inert carrier gas, which transports the liquid vapor into the reaction chamber. Volatile solids on the other hand will sublimate on arrival in the reaction chamber while gaseous precursors can be fed directly. Much like the hydrocarbon precursor, the catalyst can be used in any form as well. The catalyst can be brought into the chamber as a vapor, which is activated after undergoing pyrolysis. This is known as the floating catalyst method. A catalyst coated substrate can also be placed in the chamber before heating. This method is often used in combination with an H_2 pretreatment step, which reduces the catalyst from its oxide form to the metallic form. The catalyst on the substrate can exist in the form of a film layer or of particles. In case the film layer is thin enough, it will break up into particles when subjected to annealing. A simple representation of the basic thermal CVD is shown below in Figure 3.1.

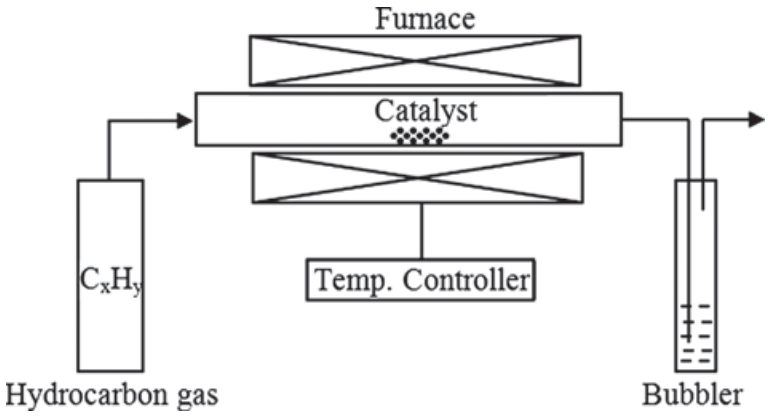

Figure 3.1: Schematic representation of a basic thermal CVD. [4]

The CVD method has a number of advantages over the arc-discharge and laser-ablation techniques, which makes it the most popular and most used method for CNT growth. First of all, the CVD method offers a lot of control and flexibility by giving the user the ability to adapt many parameters. Secondly, it is a simple and relatively economical technique. Lastly, when it comes to yield, purity and architectural control, the CVD method has the edge over the other techniques. However, CNT quality or crystallinity is inferior.

In addition to thermal CVD, there are several variants that enhance the CVD process, which involve the use of plasmas, ions, photons, lasers, hot filaments or combustion reactions. One of which is very interesting for CVD growth at lower temperatures (<600°C), namely plasma enhanced chemical vapor deposition (PECVD). This variant will be explained in more detail in the next section. [4][39][40]

3.2. Plasma Enhanced Chemical Vapor Deposition

Plasma enhanced CVD is a variation of the standard thermal CVD that, as the name implies, uses a cold plasma to assist its processes. The formation of plasma is made possible by introducing reactant gases between two parallel electrodes. One is a grounded electrode, below the substrate. The second one is an RF-energized electrode. The pulsed electrical discharges, between

these two electrodes, transforms the reactant gases into a cloud of high energetic ions, reactive radicals, neutral atoms and molecules, also known as plasma. Since the decomposition of hydrocarbons is faster and better activated by molecule collision than by thermal pyrolysis, lower process temperatures could be achieved. In addition, the presence of an electric field could enhance the alignment of the tubes. However, the ions in the plasma are accelerated to the cathode, which results in an ion bombardment of the sample. There is still uncertainty whether or not an ion bombardment is favorable for CNT growth. Figure 3.2 shows a schematic representation of a PECVD tool. [41][42][43]

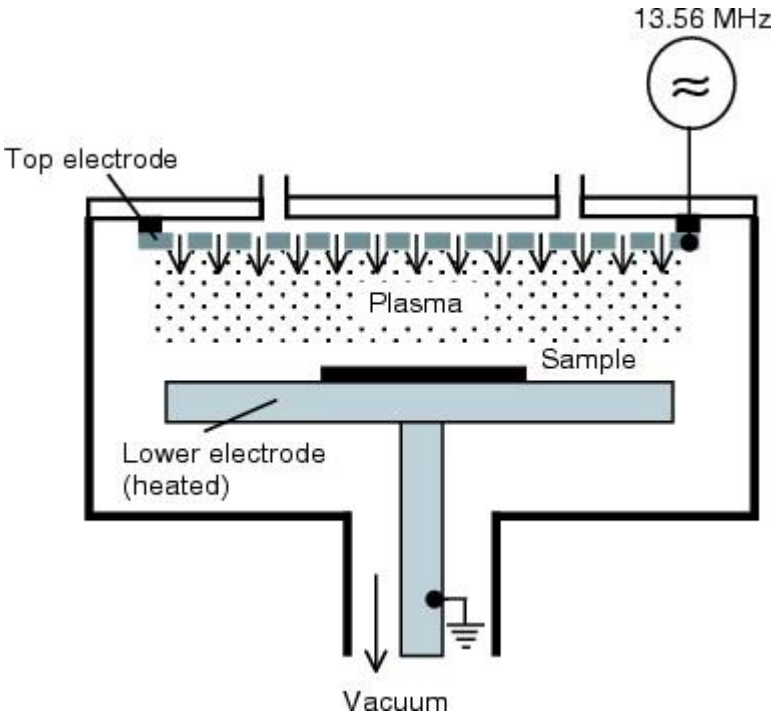

Figure 3.2: Schematic representation of a PECVD tool. [41]

4. Analysis

4.1. Scanning Electron Microscope

Compared to an everyday light microscope, a Scanning Electron Microscope (SEM) uses a beam of highly energetic electrons rather than photons, to magnify an object. The most commonly used electron source is the Field Emission Gun (FEG), which consists of a Tungsten wire with a very sharp tip (< 100nm). The FEG creates a beam of electrons, which is guided towards the sample by a combination of electromagnetic lenses and apertures. These lenses and apertures determine the acceleration rate and the spot size respectively. At the end of the column, scanning coils are used to control the position of the electron beam on the sample. These coils allow the electron beam to scan the surface and thereby collect the information that is needed for imaging. The column is kept under vacuum at all times, while the chamber can be vented to load a sample. An overview of the tool structure is shown in Figure 4.1.

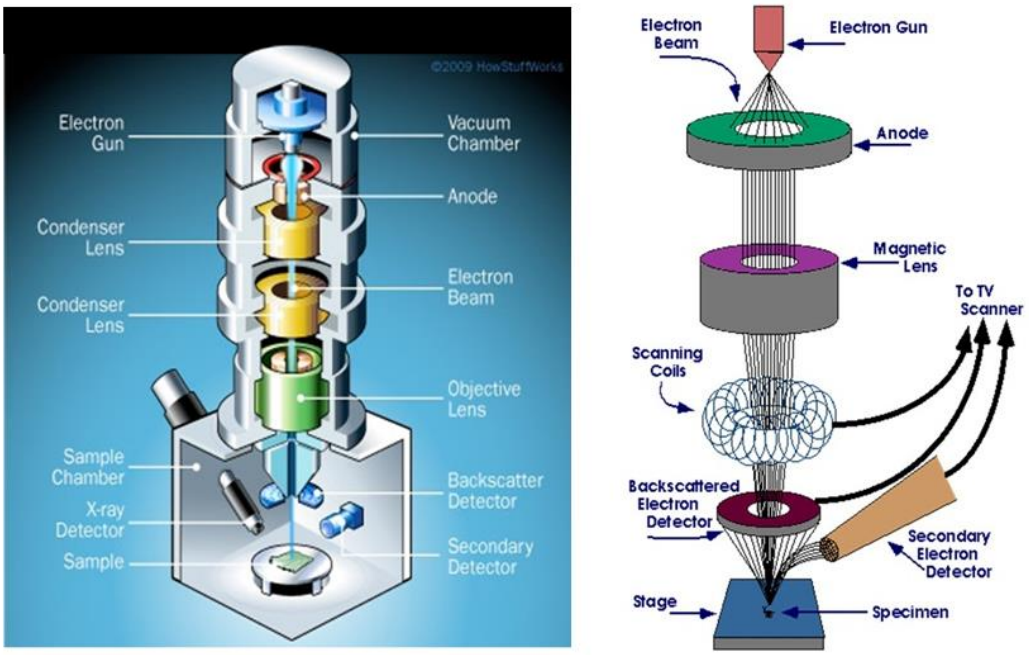

Figure 4.1: Schematic representation of a SEM tool. [44]

Once the electrons hit the solid sample and decelerate there are several kinds of electron-sample interactions, which create signals. These signals include Auger electrons, secondary electrons, backscattered electrons, diffracted backscattered electrons, photons (X-rays), visible light (CL) and heat. Each of them produce valuable information when collected in a detector. Secondary electrons (SE) are released when the electrons of surface atoms are excited by the electron beam and possess sufficient energy to leave the surface. This can lead to another phenomenon known as the Auger effect in which the resulting vacancy of the emitted SE is filled by an electron of a higher energy level. The residual energy is often released in the form of an emitted photons. However, the energy can also be absorbed by another electron, causing its ejection. This is called the Auger electron. Backscattered electrons (BSE) on the other hand are electrons from the beam that are deflected by the atom nuclei and re-emerge from the surface. As a result, heavier elements backscatter more efficiently and therefore appear brighter in an BSE image. The travel depth of BSE can be greater than that of SE. Both SE and BSE are mainly used for imaging. While SE is especially valuable for showing morphology and topography, BSE is more valuable to illustrate contrast in sample composition as mentioned earlier. Diffracted backscattered electrons (EBSD) are mainly used to determine crystal structures. At last, X-rays are produced when an inelastic collision occurs between a beam electron and an electron in the lower shells of a sample atom. When the excited electron returns to a lower energy state, they release element specific X-rays. Hence, X-rays are used for element analysis. The acceleration rate of the e-beam determines the electron-sample interaction and therefore the signal type. All possible signal types with their place of origin are shown below in Figure 4.2.

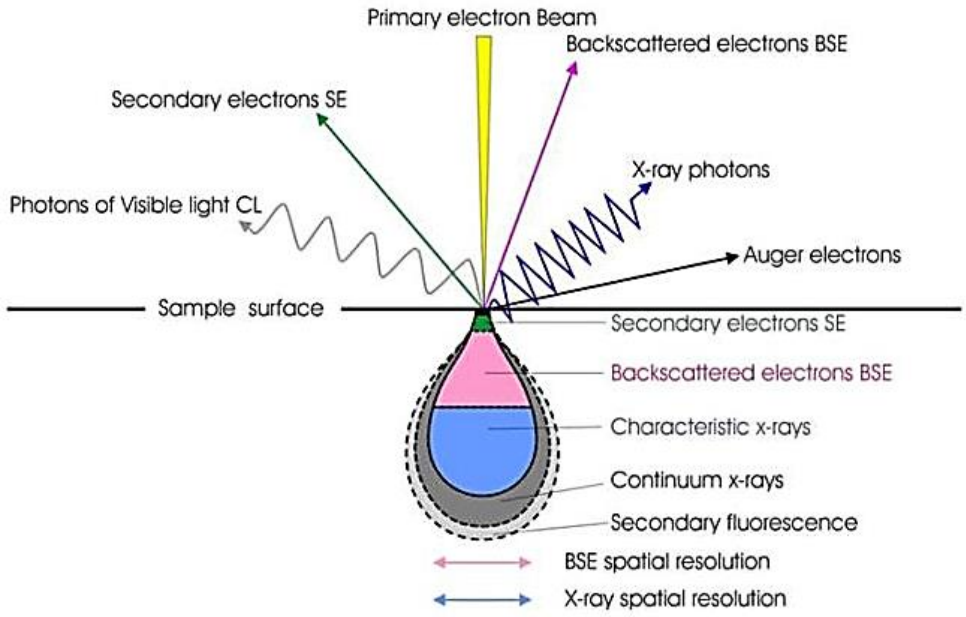

Figure 4.2: All signal types with their place of origin. [45]

In theory, SEM analysis is often nondestructive, meaning that it does not lead to volume loss. However, in the case of CNTs the morphology can change to amorphous carbon due to the highly energetic electron bombardment and charging of the sample as the electron cannot be released on time. This can be avoided to some extent by adjusting the voltage and spot size. [46][47][48][49][50]

5. Experiments & Discussion

All experiments are carried out with the 'Oxford Instruments Plasmalab System 100 PECVD'. Sample inspection and analysis is performed with the 'FEI Nova NanoSEM 200'.

5.1. Context

This research is conducted within the framework of CNT interconnects. The end goal of this research is to find out if and how traditional copper interconnects in today's chips could be replaced by their CNT counterparts in the future. The target is to develop the best possible CNT growth recipes on Ni/TiN (catalyst/substrate) at different temperatures. To reach this goal, a better understanding of each growth parameter is needed and how these parameters influence each other. However, because this technology needs to be CMOS compatible for on-chip fabrication, there are several restrictions to be taken into account.

The CMOS restrictions on CNT growth are the followings:

- The wafer temperature should be kept below 420°C at all times due to the risk of transistor damage (back end of line).
- The substrate must be conductive to achieve good interconnects, which means no oxides can be used as a substrate for CNT growth.
- Certain catalysts ,that are not CMOS compatible, like Fe and Au cannot be used in order to avoid transistor damage.
- The nanotubes need to be grown on wafers
- The process time and cost must be taken into account
- The growth process should minimize contamination in subsequent processing (adhesions, growth residuals, ...), for the environment, people and tools.

Apart from the CMOS restrictions, there are also restrictions regarding the PECVD tool, such as the availability of certain gases, maximum temperature, maximum flow, etc… Some of these tool characteristics are listed below:

- Available process gases: CH_4, C_2H_2, NH_3, H_2, N_2, O_2, Ar.
- Temperature range: 0^oC - 800^oC.
- Total pressure range: Vacuum ($\approx 10^{-6}$ T) – 10 T.
- Plasma range: 0W – 300W (at a 13.56 MHz discharge).
- Maximum flow rate (sccm):
  - CH_4: 100
  - C_2H_2: 100
  - NH_3: 100
  - H_2: 200
  - N_2: 1000
  - O_2: 100
  - Ar: 1000
- Helium purge range: 2.1 T – 10 T.

The course of this study is explained in a chronological order to better understand why certain experiments were carried out. It should be noted that this thesis represents only three weeks of CNT growth work due to technical problems with the PECVD tool. However, interpretation and evaluation of the samples was distributed over a longer period.

All growth experiments are executed on 0.8nm Ni / 70nm TiN blanket coupons (2x2cm).

5.2. Pretreatment and growth

The CNT growth process on Ni/TiN blankets is divided into two parts. The first part consists of the pretreatment step, which, through a thermal anneal,

breaks up the nickel film into particles. This pretreatment step can be assisted by plasma. After the initial particle formation, the particle size will start to increase through coalescence or through the Ostwald ripening effect. The pretreatment step is followed by the carbon deposition step, also referred to as the growth step. At this point a carbon precursor is introduced into the process chamber, which entails an incubation period. Once the state of supersaturation is reached, the actual growth is initiated. The course of the CNT growth process using blankets is shown in Figure 5.1.

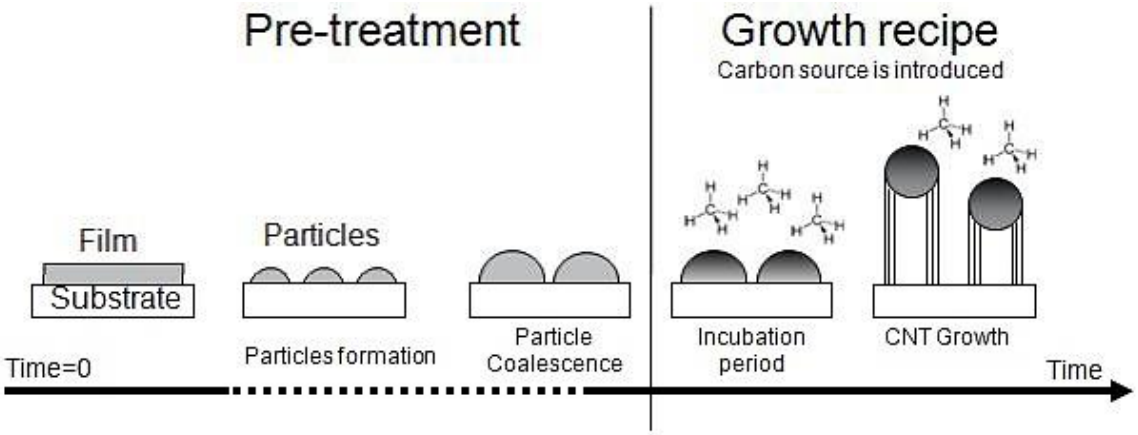

Figure 5.1: The course of the CNT growth process using blankets. [35]

5.3. Temperature calibration

The temperature in the PECVD tool is calibrated using a thermal track wafer. This 200 mm silicon wafer features five thermocouples spread over its surface, which measure the temperature on top of the wafer while the wafer is in contact with the heater. The temperature is sensitive to the total pressure, whereby the temperature is proportional to the pressure due to better heat transport. In addition, the actual temperature is always lower than the set temperature due to the heat distribution and imperfect contacts between the wafer and the heater. The temperature uniformity over the full 200 mm wafer is good, with a maximum center to edge wafer temperature variation of 15°C. A linear correlation is found between the set and actual temperature for the three datasets. At lower set temperatures, the difference

between set and actual temperatures are lower as less energy needs to be transferred from the heater to the wafer. When operating at 4 Torr, the average drop in temperature is ~50°C. The temperature measurements are executed for 1 Torr, 4 Torr and 8 Torr. The result for 2 Torr is calculated based on the existing data. The relation between set temperature and actual temperature at different total pressures is shown in Graph 5.1.

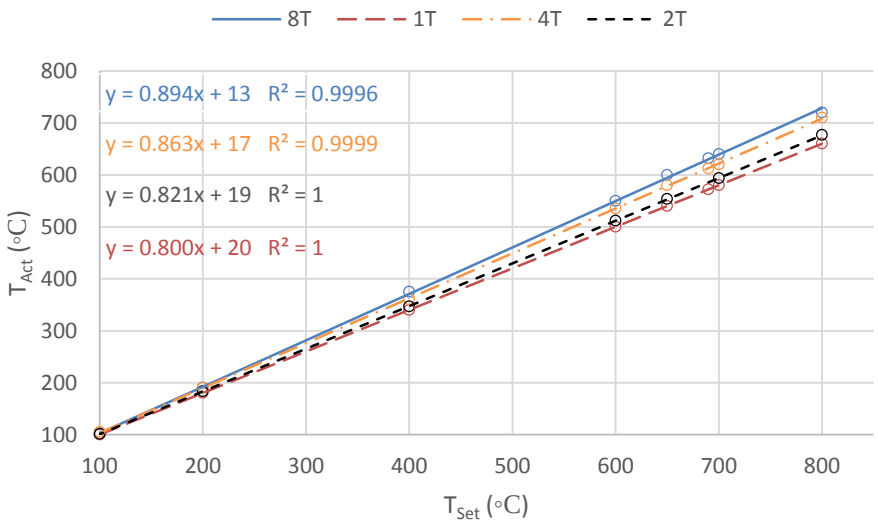

Graph 5.1: Average temperature of the pocket wafer in function of the set temperature for different total pressures: 1 Torr, 2 Torr, 4 Torr and 8 Torr.

The same data is also used to determine the actual on-wafer temperature when a different total pressure is used for a certain set temperature. The result for 690°C is not obtained directly from the measured data, but it is calculated based on them. The relation between the actual temperature and the total pressure at different set temperatures is shown in Graph 5.2.

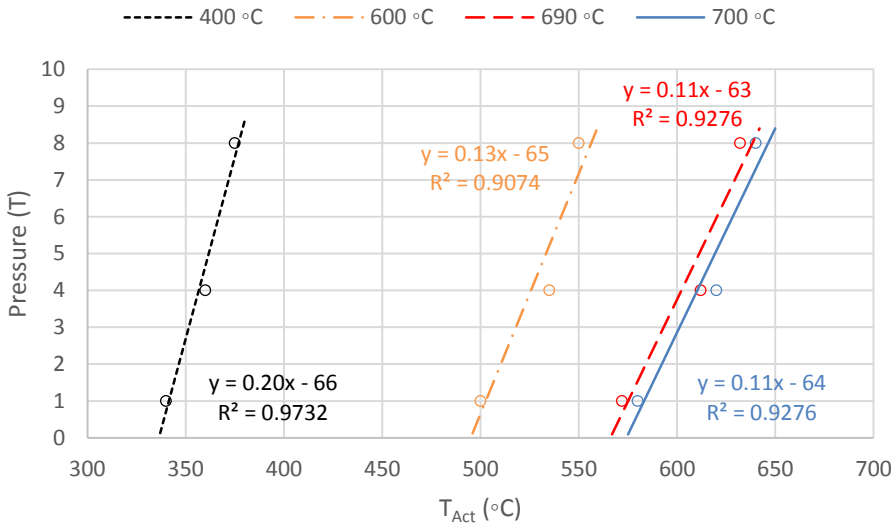

Graph 5.2: Average temperature of the pocket wafer in function of the total pressure for different set temperatures: 400°C, 600°C, 690°C, 700°C.

The experiments in this work are performed at a coupon level (20 x 20 mm in size). The CVD tool uses a robot arm for transporting the material to the chamber. This robot arm can only carry large samples, such as 200 mm wafers. In order to be able to process coupons, a carrier wafer is used containing a pocket in which the coupons are placed. These two graphs are used in this work to correlate the set temperature to the actual temperature of the pocket wafer used to carry the samples in the tool. Due to the extra interface, additional temperature losses need to be taken into account. The sample temperature, when placed on top of the carrier wafer, is expected to be ~20°C lower. To minimize possible sample to sample variations, the samples were always placed in the center of the wafer. For the following experiments a pocket wafer was used, which has a deepened center (half of the original wafer thickness) with the aim to approximate processed wafer conditions. Therefore the loss in temperature is expected to be ~10°C. instead of ~20°C. The resulting temperature drop arising from the set-to-actual temperature difference plus the pocket wafer is usually in the order of ~60°C when working at 4T.

5.4. Startup and reference run

In idle state, the heater of the CVD tool is kept at room temperature. During operation, the heater is cooled with water to ensure endurance. The startup of the PECVD tool involves heating the process chamber for 30 minutes using the following parameters:

- Gas flow: 500 sccm N_2 / 6 sccm He purge
- Temperature: 690°C or the one desired
- Total pressure: 1000mT
- No plasma

Before every growth session, at least one reference run is executed on 1 nm Ni / 70 nm TiN blanket coupons with a standard recipe to check for technical problems and confirm reproducibility of the tool. The reference recipe is given below in Table 5.1.

Table 5.1: Reference recipe.

Ref	Pretreatment						Carbon Deposition						
Set °C	Sccm	Sccm	Torr	M' S''	Act °C	Sccm	Sccm	Sccm	Pressure		M' S''	Act °C	Sccm
Temp	**H_2**	**Ar**	**Press**	**Time**	**Temp**	**He**	**C_2H_2**	**Ar**	**Tot(T)**	**Part(mT)**	**Time**	**Temp**	**He**
690	200	600	4	5'	613	6	5	495	4	40	10'	613	6

5.5. Disclaimer

All analysis are done with an uncalibrated SEM, therefore the measured lengths and widths cannot be taken as actual values at a sub 10 nm level. They can however be used to derive relations. Processing of the results regarding the width are even more prone to errors due to the randomness of the measurements. In general, five to six CNTs are measured of which the middle value is estimated. Since CNT widths can differ significantly and the choice in which nanotube to measure is subjective, the number that is portrayed can give a biased picture of reality.

Because CNT growth conditions are tool dependent, it is safer to only compare results that were carried out on the same tool, therefore all results are compared with the work of N. Chiodarelli (Ph.D. thesis at imec 2010). General trends and observations are put in perspective with other work from literature.

5.6. Growth session 1: Pretreatment

The focus of the first growth series to find a good catalyst pretreatment recipe. The main goal is to compare different pretreatment recipes while maintaining the same temperature and growth recipe. The experiments are performed at four different temperatures with the use of four different pretreatment recipes namely, NH_3 plasma-, H_2 plasma-, thermal- and no pretreatment. A description of the recipes can be found in Table 5.2, while the qualitative and quantitative results are shown in Table 5.3.

The recipes are arranged according to decreasing temperature. The color code in the tables is as follows: blue represents plasma pretreatment, white represents thermal pretreatment and red represents no pretreatment. This applies to all tables given in this report.

In some tables the flow of the helium purge is not mentioned as it is a constant set value. The He flows from the heater to the substrate and creates a thin film to protect the heater and promote a good heat transfer. In general, the flow of the helium purge is chosen in function of the total pressure. The following rule applies:

- 4 Torr and below: 6 sccm He
- 8 Torr: 10 sccm He

Table 5.2: Pretreatment and growth recipes for session 1.

01		Pretreatment							Carbon Deposition					
	Set ºC	Sccm	Sccm	Sccm	HF (W)	Torr	M' S''	Act ºC	Sccm	Sccm	Pressure		M' S''	Act ºC
Sample	Temp	H_2	NH_3	Ar	Plasma	Press	Time	Temp	C_2H_2	Ar	Tot(T)	Part(mT)	Time	Temp
01	690	-	100	-	100	1	2'30"	572	5	495	4	40	10'	613
02	690	200	-	600	100	1	2'30"	572	5	495	4	40	10'	613
03	690	200	-	600	-	4	5'	613	50	450	4	400	10'	613
04	690	200	-	600	-	4	5'	613	5	495	4	40	10'	613
05	690	-	-	-	-	-	-	-	5	495	4	40	10'	613
06	650	200	-	600	-	4	5'	579	50	450	4	400	10'	579
07	650	200	-	600	-	4	5'	579	5	495	4	40	10'	579
08	650	-	-	-	-	-	-	-	5	495	4	40	10'	579
09	600	-	100	-	100	1	2'30"	500	5	495	4	40	10'	535
10	600	200	-	600	100	1	2'30"	500	5	495	4	40	10'	535
11	600	200	-	600	-	4	5'	535	5	495	4	40	10'	535
12	550	200	-	600	-	4	5'	492	5	495	4	40	10'	492

Note that the duration of the growth step is set to 10 minutes in session 1 whereas the other growth sessions have a carbon deposition time of 15 minutes (starting from Table 5.4). In order to compare CNT lengths of growth sessions mutually, the CNT length of session 1 are corrected to a 15 minutes timeframe. From previous work, it is found that for short CNT growth times (< 30 minutes) the length can be linear proportional to the growth time. Therefore the CNT lengths for the 10 min. recipes are extrapolated to 15 min. to allow for a direct comparison when needed. Time-corrected lengths are marked in red. In all following comparisons, the time-corrected length will be used.

Table 5.3: Growth results of session 1.

Sample	Best/ Temp	Visual Quality	Comment	Alignment	Yield	°C$_{set}$	Length µm	Corr. Length	Diam. nm ±5
01		3	Curly bottom	straight	okay	690	2.6	3.9	16
02			No growth	none	none	690	0.0	0.0	0
03		2	Length differences	spagh.	poor	690	1.4	2.1	14
04		4	Curly bottom	straight	okay	690	3.7	5.6	12
05	X	4	Dense growth	straight	good	690	3.5	5.3	16
06		4	Length differences	spagh.	poor	650	1.3	2.0	22
07		2	Large diameter distribution	spagh.	okay	650	1.0	1.5	13
08	X	4	Fat CNT top	straight	good	650	1.3	2.0	11
09	X	4	Fat CNT top	straight	okay	600	1.6	2.4	17
10		1	Small diameter distribution	curked	okay	600	1.1	1.7	14
11		4	Very curly	spagh.	okay	600	1.2	1.8	15
12	X	4	Fat CNT top	straight	good	550	1.6	2.4	12

Legend	
1 2 3 4	Alignment: packed > straight > curled > spaghetti > none Yield: good > okay > poor > none

5.6.1. Influence of the pretreatment type at constant temperature

In this part several pretreatment types will be compared at a constant set temperature. This is done for three temperatures, ranging from 600°C to 690°C. First, a visual comparison will be made based on SEM images, after which a quantitative analysis is done based on CNT length and diameter. All recipes used in this comparison can be found in Table 5.2. Note that recipes 03 and 06 will not be discussed in this part due to a difference in partial pressure of acetylene in the growth step, while recipe 06 from session 2 is added to this comparison (Table 5.4).

At 690°C the pretreatment types yield very different results (Figure 5.2). The NH_3 plasma pretreatment yields nanotubes of a decent length compared to H_2 plasma. However, the alignment is only moderately upright and suffers from a very curly region at the bottom of the forest. Further upwards, the tubes are more straightened. The H_2 plasma pretreatment on the other hand yields no growth at all. This is in agreement with the findings of N. Chiodarelli. Thermal and no pretreatment yield the best results. While the length is similar, the alignment is not. While being fairly straight aligned, the thermal pretreatment results in a forest which features small curls over the entire length of the tubes. These curls are not present in the no pretreatment forest. In conclusion, it is fair to say that at 690°C no pretreatment delivers the best result. The anneal itself seems to be enough to break up the nickel blanket and activate the catalyst, whereas plasma pretreatments seem to partially or completely deactivate the catalyst.

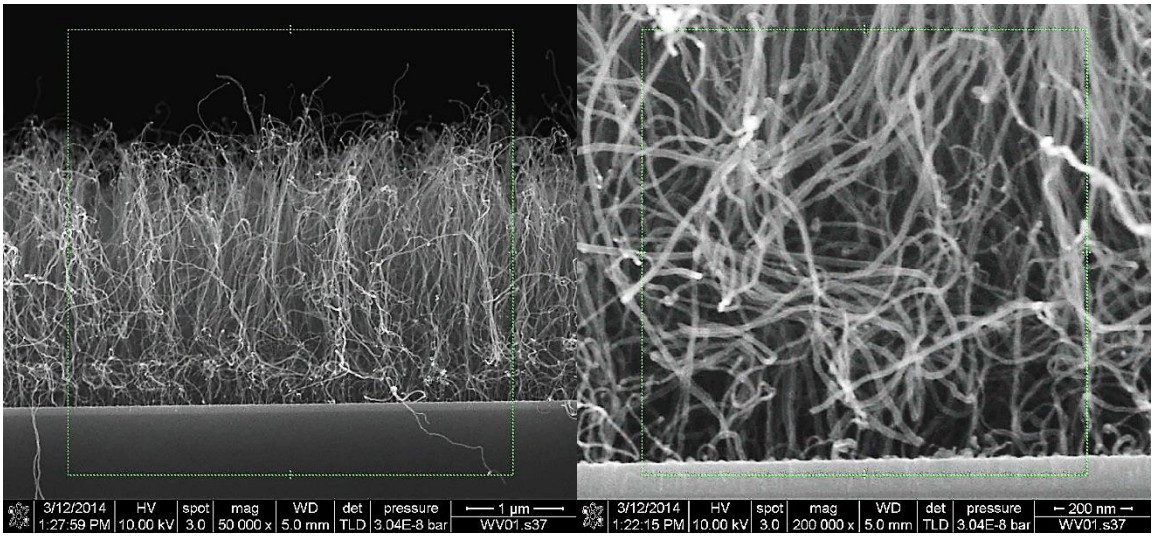

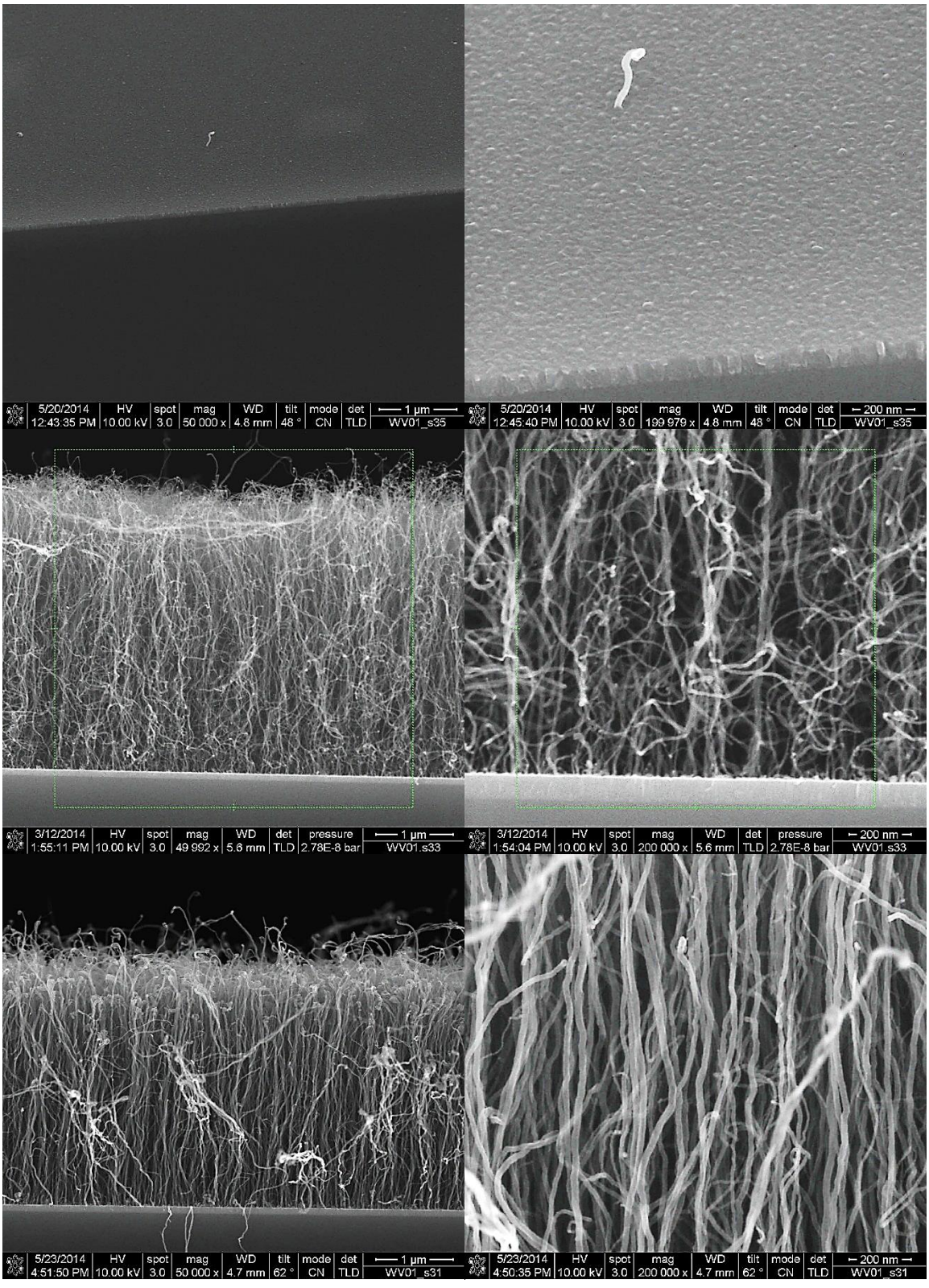

Figure 5.2: XSEM images of CNT growth with all four pretreatment types at a set temperatures of 690°C (Table 5.2) with (left) growth overview and (right) zoom in. Sample order from top to bottom: 01.01 NH_3 plasma, 01.02 H_2 plasma, 01.04 Thermal and 01.05 No-PT.

At 650°C only two pretreatment types are executed, i.e. thermal and no pretreatment. Although the yield delivered by both pretreatments are not great, they differ significantly. The thermal pretreatment continues to result in a rather curly forest (Figure 5.3). However, unlike at 690°C, the lower temperature does not allow the forest to take on a straight alignment; instead, it features a spaghetti like conformation. In the case no pretreatment is used, the forest remains straight to some extent. However, the forest is divided into two parts. The lower part is very thin and curly, whereas at the upper part the tubes become fat and less curly. This phenomenon will return several more times and will now be referred to as the smoke structure because of the resemblance with smoke coming out of a cigarette, thin and curly at the base, wide and straight at the top. Based on SEM alone, the no pretreatment forest could be considered to be the better one.

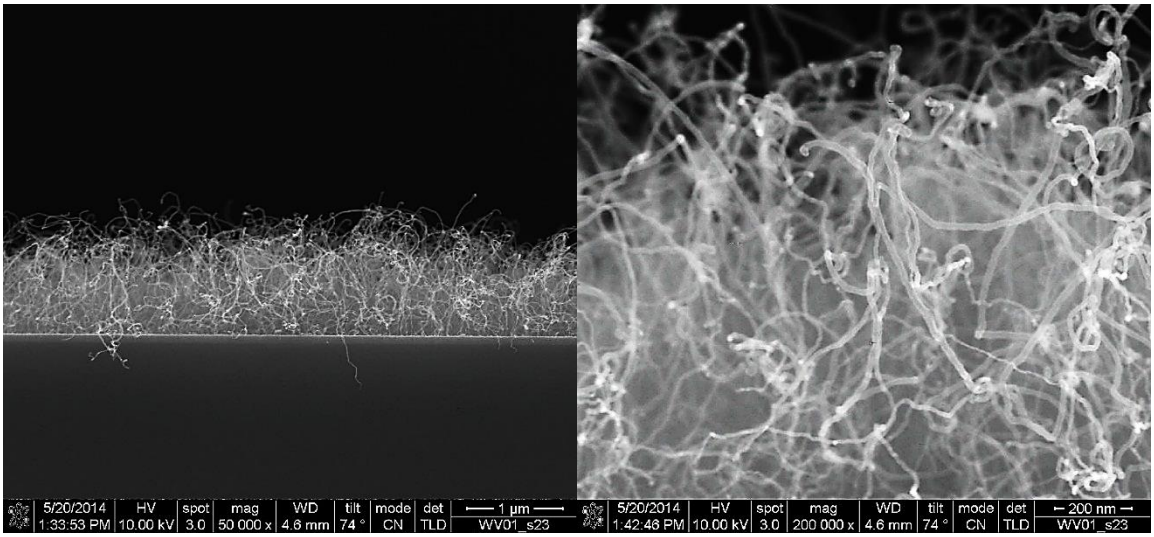

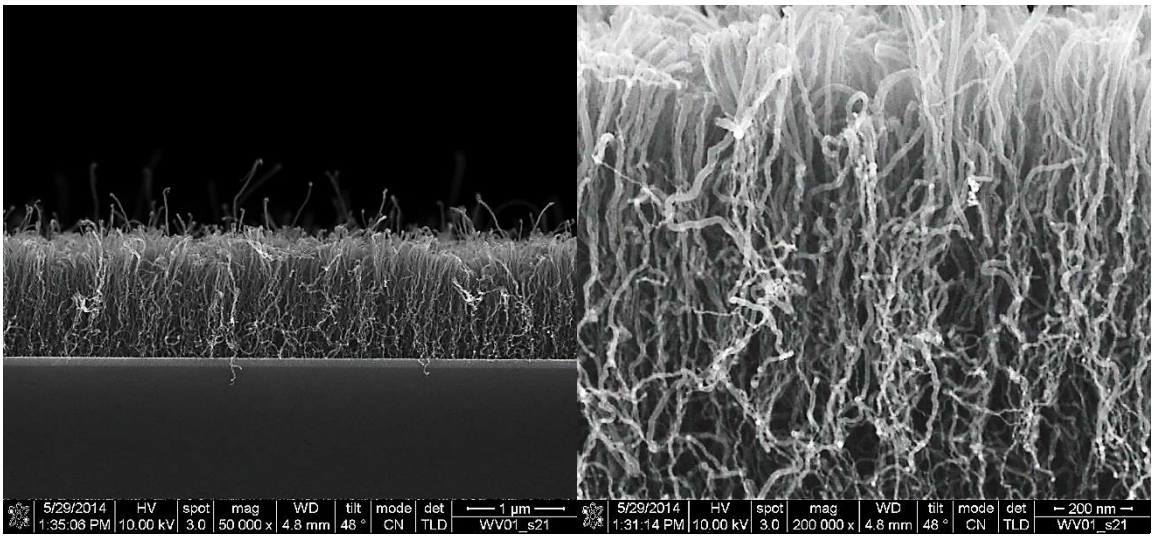

Figure 5.3: XSEM images of CNT growth with two pretreatment types at a set temperatures of 650°C (Table 5.2) with (left) growth overview and (right) zoom in. Sample order from top to bottom: 01.07 Thermal, 01.08 No-PT.

At 600°C, all four pretreatment types are discussed. The NH_3 plasma- and no pretreatment suffer from the same smoke-like structure as the no-pretreatment recipe at 650°C (Figure 5.4). This pattern returns in the H_2 plasma and thermal pretreatments as well, although to a lesser extent. However, the NH_3 plasma- and no pretreatment forests are the only ones to retain a certain straightness and therefore could be considered to be the better recipes at 600°C.

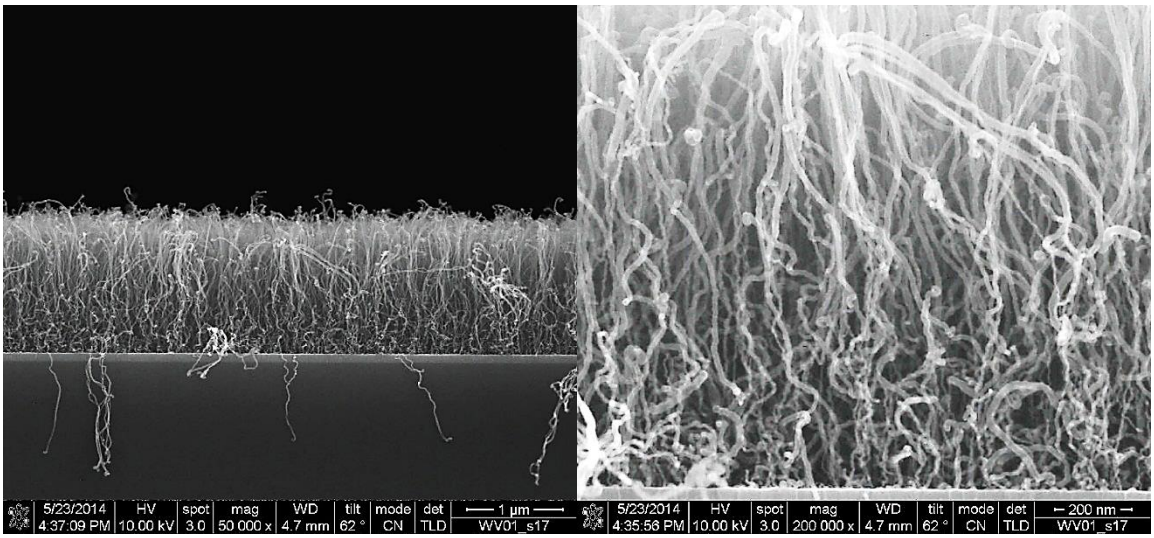

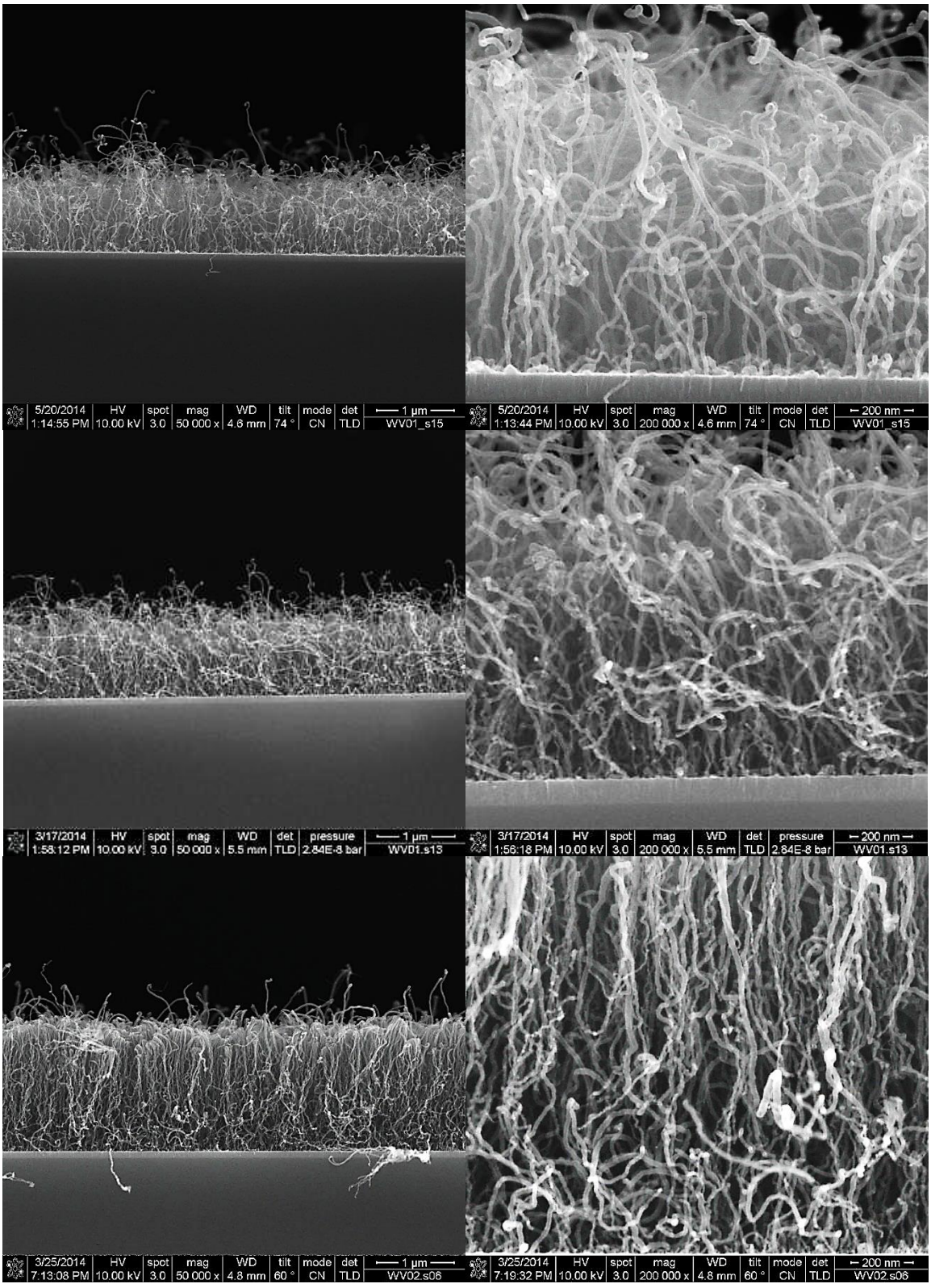

Figure 5.4: XSEM images of CNT growth with all four pretreatment types at a set temperatures of 600°C (Table 5.2 and Table 5.4) with (left) growth overview and (right) zoom in. Sample order from top to bottom: 01.09 NH_3 plasma, 01.10 H_2 plasma, 01.11 Thermal and 02.06 No-PT.

By plotting the CNT length towards the set temperature, two interesting observations can be made (Graph 5.3). First, the evolution of the length can be followed over a certain temperature range, for each pretreatment type. Second, the best pretreatment type can be observed for a specific temperature. The evolution of all four pretreatments show that, irrespective of the pretreatment type itself, the temperature is a determining factor for growth. By focusing on the plasma pretreatments, it can be stated that overall NH_3 plasma seems to preserve the catalytic activity better than H_2 plasma at high temperatures. This is in agreement with the findings of N. Chiodarelli. Although, more data is needed to see whether or not H_2 plasma can overtake NH_3 plasma at lower temperatures. Thermal- and no pretreatment seem to follow the same downward course at first. However, the thermal pretreatment seems to recuperate at lower temperatures. Based on these results we decided to further examine the possibilities of the thermal- and NH_3 plasma pretreatments in growth session 2. Note that the no pretreatment recipe from session 2 (600°C) is added to this comparison.

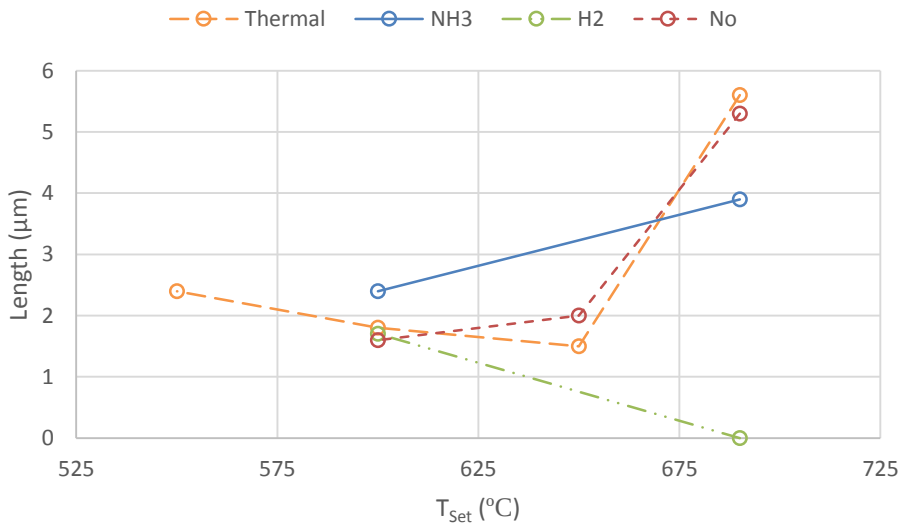

Graph 5.3: CNT length in relation to set temperature for all four pretreatment types.

Despite the few data, plotting the CNT diameter towards the set temperature shows that NH_3 plasma yields wider CNTs than H_2 Plasma (Graph 5.4). This corresponds to the findings of N. Chiodarelli. He showed that NH_3 plasma

yields bigger catalyst particles than H_2 plasma. Since the CNT diameter and the particle size are related this statement could be valid. However, judging from only two data points it could as well be coincidence. What concerns the thermal pretreatment, the diameter remains fairly stable, while the diameter of the no pretreatment recipes fluctuates stronger.

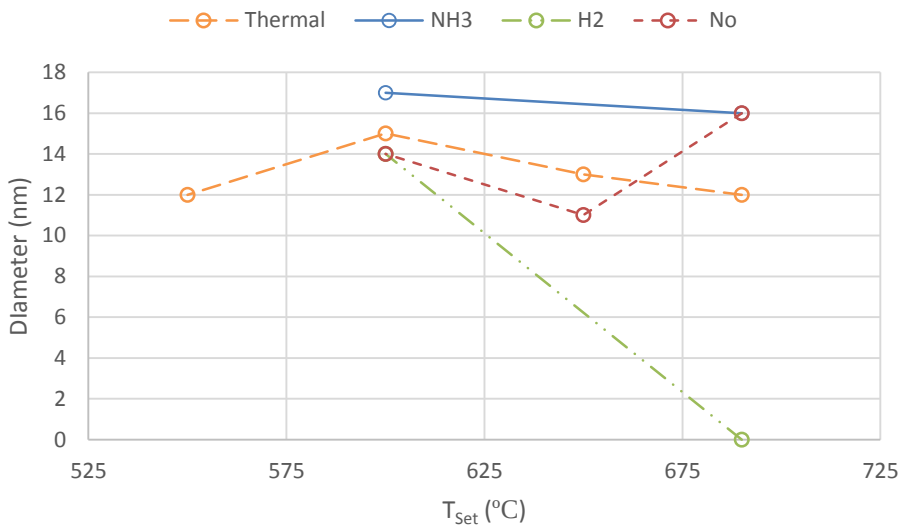

Graph 5.4: CNT diameter in relation to set temperature for all four pretreatment types.

5.6.2. Influence of the temperature on the no-pretreatment recipe

In this comparison, the influence of the temperature is examined, using one specific recipe at a range of different temperatures. The growth recipe used is the same as the no pretreatment recipe in growth session 1, executed at the following temperatures: 800°C and 750°C (Table 5.6), 690°C and 650°C (Table 5.2), 600°C (Table 5.4).

Note that for all recipes performed at temperatures above 690°C, the samples spend more time in the process chamber due to a two-step process. The sample is loaded into the chamber at 690°C, followed by a heating step to the desired temperature. To unload the sample this step is reversed, thus cooling the sample to 690°C before unloading. This two-step process is put into place to ensure that the temperature difference between the loadlock

and the process chamber does not get too high. In case this happens, the graphite electrode within the chamber might get oxidized. The additional time spent in the process chamber for recipes at 750°C is 5 minutes, while for processes at 800°C it raises to 8 minutes.

Since the pretreatment step is absent in every recipe, this comparison revolves more around how the temperature relates to the growth parameters. Therefore, it is possible to determine at which temperature this specific recipe yields the best results. At 800°C the growth turns out to be spaghetti-like with a lot of length differences between the tubes (Figure 5.5). Shorter, immature tubes can be observed at the bottom. These conditions return at 750°C to some extent. Although the forest is longer and better aligned, the curled bottom is even more present and the length differences are maintained. At 690°C, the best growth in this series is achieved. The forest is long and well aligned with a fairly small length distribution. At 650°C however, the length and quality start to decline again, with the now known smoke conformation. An almost identical forest structure is found at 600°C. It seems that for these conditions a temperature optimum exists around 690°C.

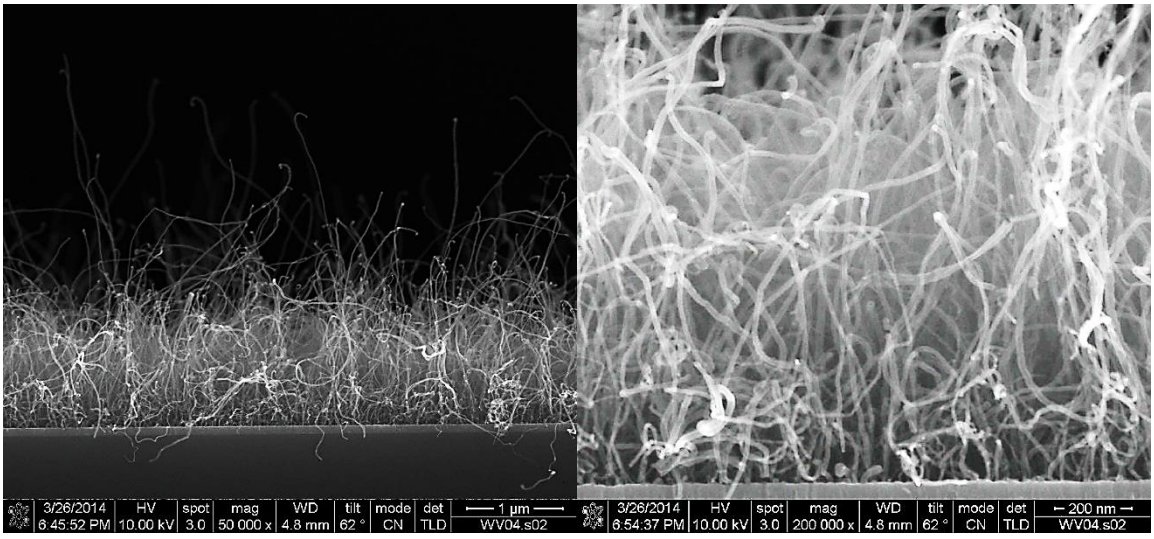

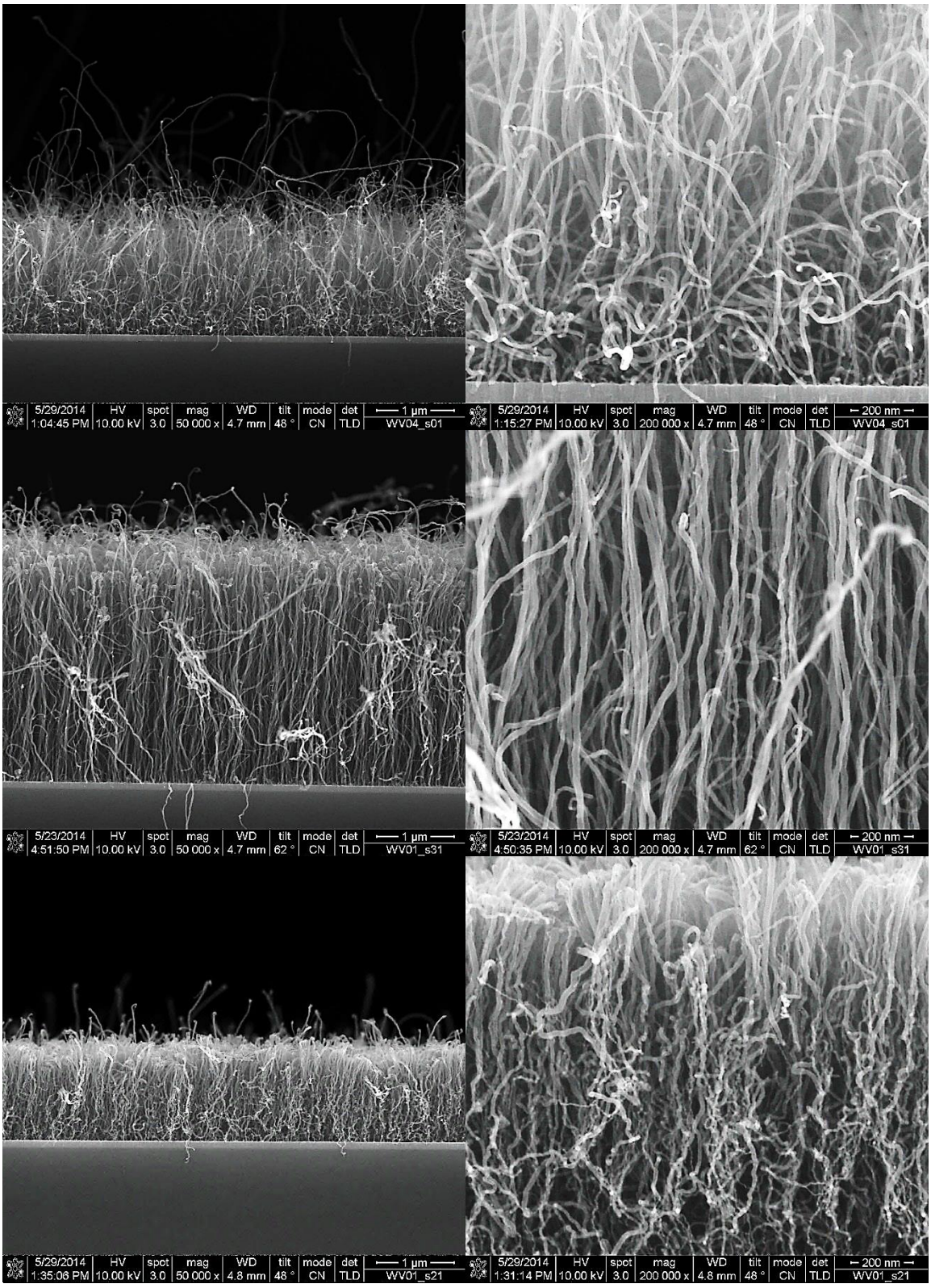
5/29/2014 | HV | spot | mag | WD | tilt | mode | det | 1 µm | WV04_s01
1:04:45 PM | 10.00 kV | 3.0 | 50 000 x | 4.7 mm | 48 ° | CN | TLD
5/29/2014 | HV | spot | mag | WD | tilt | mode | det | 200 nm | WV04_s01
1:15:27 PM | 10.00 kV | 3.0 | 200 000 x | 4.7 mm | 48 ° | CN | TLD
5/23/2014 | HV | spot | mag | WD | tilt | mode | det | 1 µm | WV01_s31
4:51:50 PM | 10.00 kV | 3.0 | 50 000 x | 4.7 mm | 62 ° | CN | TLD
5/23/2014 | HV | spot | mag | WD | tilt | mode | det | 200 nm | WV01_s31
4:50:35 PM | 10.00 kV | 3.0 | 200 000 x | 4.7 mm | 62 ° | CN | TLD
5/29/2014 | HV | spot | mag | WD | tilt | mode | det | 1 µm | WV01_s21
1:35:06 PM | 10.00 kV | 3.0 | 50 000 x | 4.8 mm | 48 ° | CN | TLD
5/29/2014 | HV | spot | mag | WD | tilt | mode | det | 200 nm | WV01_s21
1:31:14 PM | 10.00 kV | 3.0 | 200 000 x | 4.8 mm | 48 ° | CN | TLD

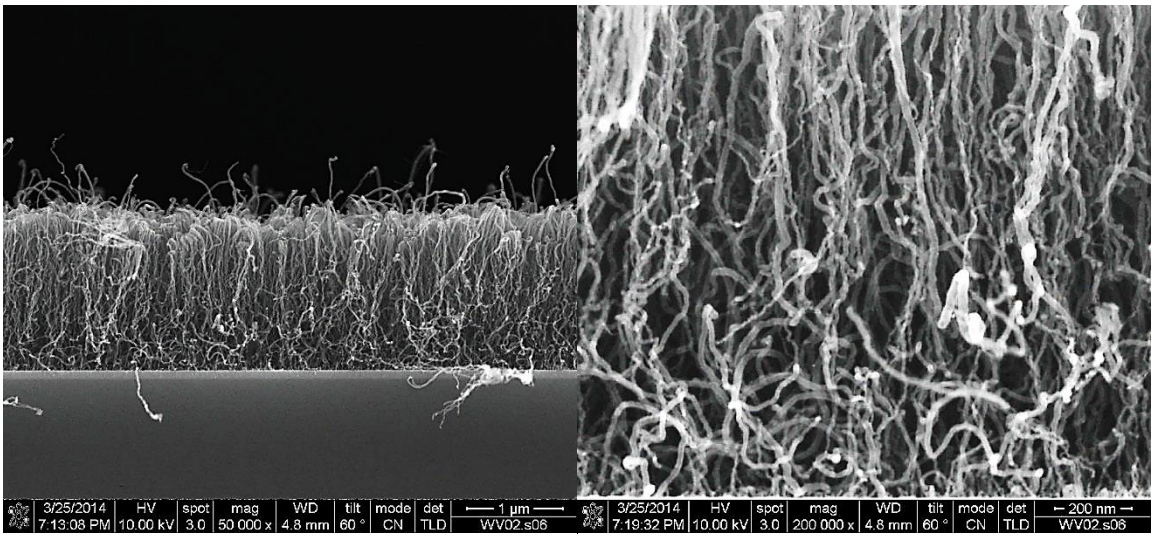

Figure 5.5: XSEM images of CNT growth without pretreatment at a range of set temperatures of 600°C (Table 5.2, Table 5.4 and Table 5.6) with (left) growth overview and (right) zoom in. Sample order from top to bottom: 3/4.09 800°C, 3/4.08 750°C, 01.05 690°C, 01.08 650°C, 02.06 600°C.

When plotting the CNT length towards the set temperature, the same temperature optimum is observed (Graph 5.5). While the decline in growth at lower temperatures is not surprising, the disappointing yield at higher temperatures is interesting. Two possible explanations could clarify this behavior. First of all, it is well known that the decomposition rate of the carbon precursor increases with temperature, which could cause catalyst poisoning to occur faster. Secondly, the mobility of the catalyst particle increases with temperature, which means that at higher temperatures coalescence and the Ostwald ripening effect start to play a bigger role. This would result in an increase in particle size and therefore incubation time.

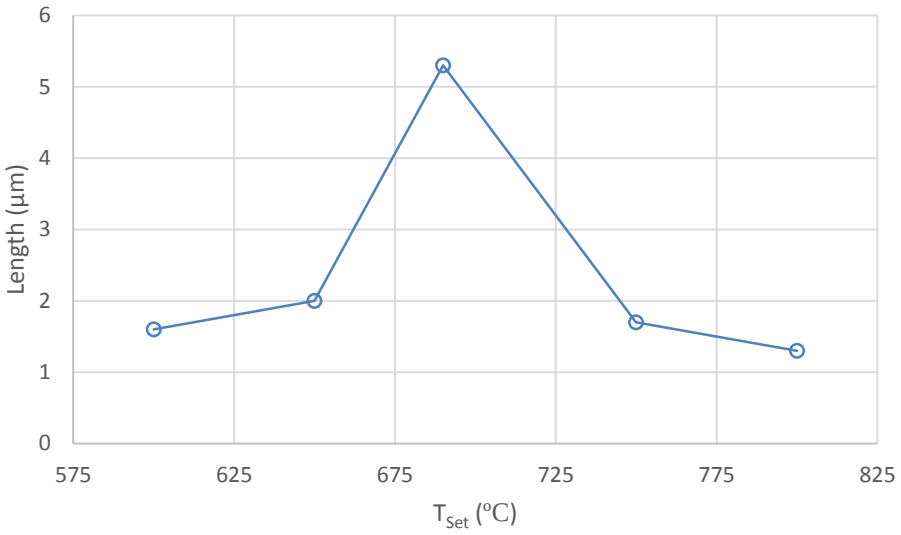

Graph 5.5: CNT length in relation to set temperature for the No-PT growth recipe.

Although observations like this have been reported before, repeating this experiment over a broader temperature range for different recipes could hold valuable information regarding the influence of different parameters on the catalytic activity. [51]

5.6.3. Influence of the partial pressure on the thermal pretreatment recipe

This comparison revolves around a difference in partial pressure during the growth step. The experiment is carried out at two different temperatures, 690°C and 650°C. The samples referred to are 01.03, 01.04, 01.06 and 01.07, and can be found in Table 5.2.

At 690°C, the difference in growth is notable. At a partial pressure of 400 mTorr the forest turns out to be short and spaghetti-like, while being relatively straight, long and dense at 40 mTorr (Figure 5.6).

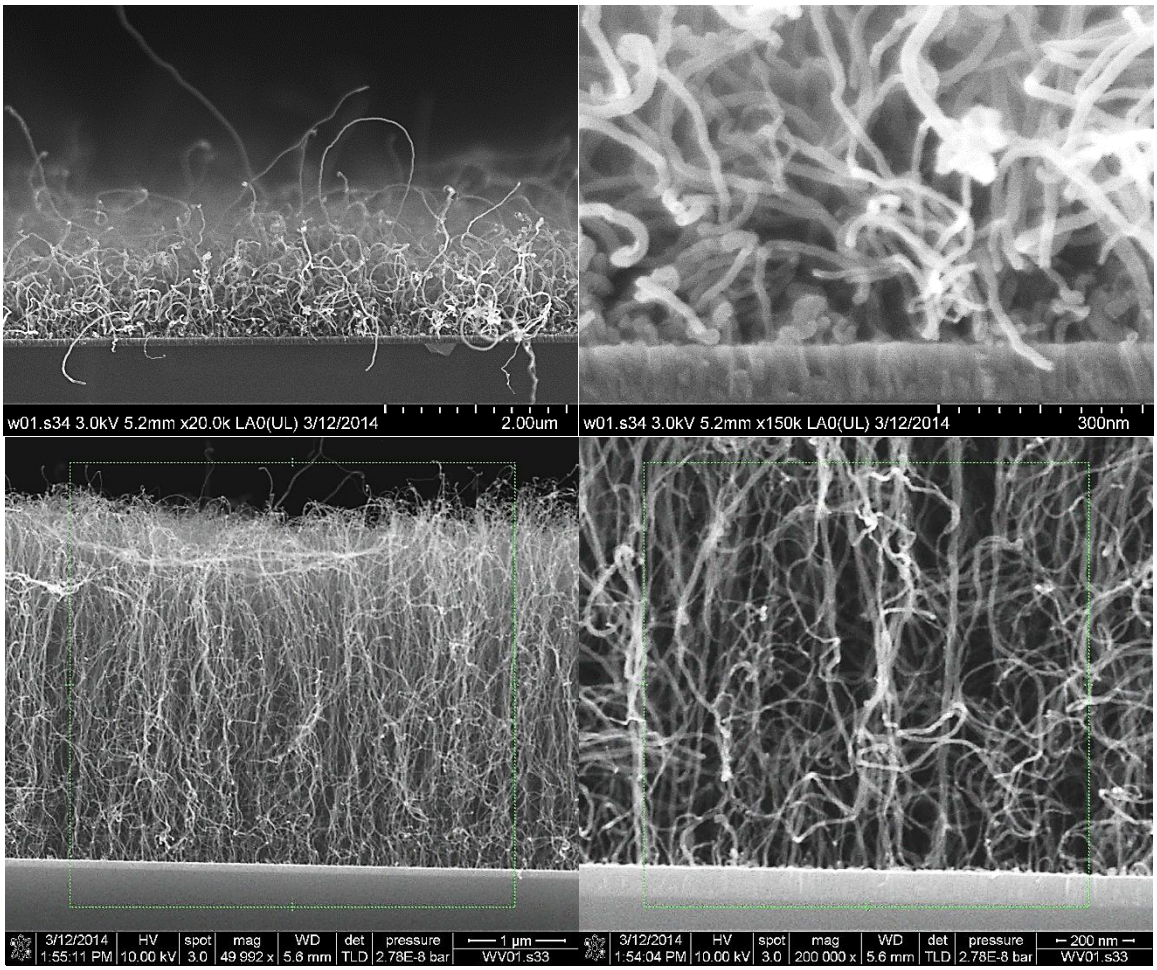

Figure 5.6: XSEM images of CNT growth with two different partial pressures at a set temperatures of 690°C (Table 5.2) with (left) growth overview and (right) zoom in. Sample order from top to bottom: 01.03 400mT, 01.04 40mT.

At 650°C however, the situation is somewhat different. At a partial pressure of 400 mTorr, the forest remains similar to the one at 690°C, whereas at 40 mTorr the growth is worsened dramatically (Figure 5.7). Despite the change in ratio, the lower partial pressure retains the upper hand, in both forest quality and quantity.

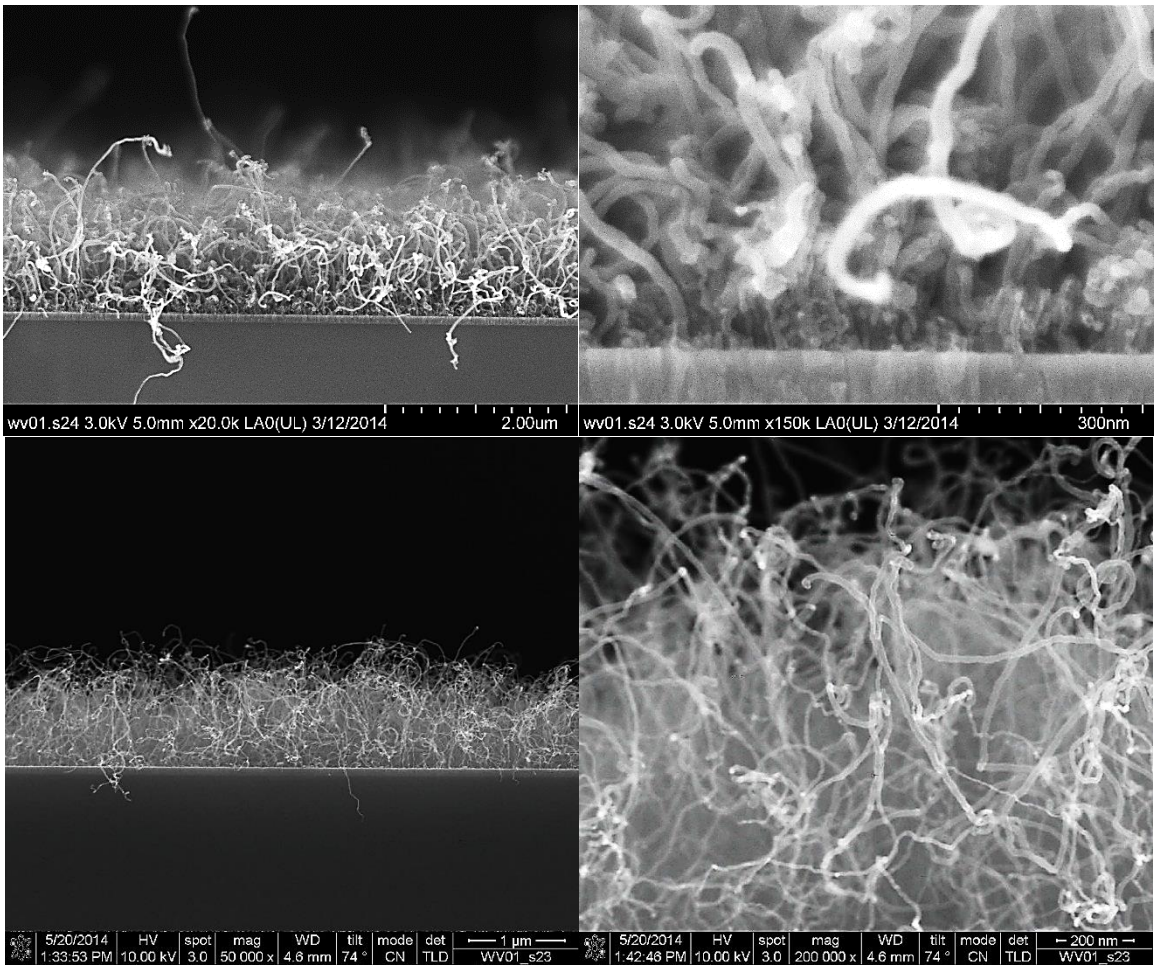

Figure 5.7: XSEM images of CNT growth with two different partial pressures at a set temperatures of 650°C (Table 5.2) with (left) growth overview and (right) zoom in. Sample order from top to bottom: 01.06 400mT, 01.07 40mT.

Plotting the CNT length towards the set temperature shows the evolution in length over two temperatures for both partial pressure recipes. The length at 400 mTorr seems to remain constant over temperature, while for the 40 mTorr recipe an increase in length is observed (Graph 5.6). Based on Graph 5.6, one could get the impression that at lower temperatures higher partial pressures yield better growth. However, based on the SEM images, this is clearly not the case. Since the length of spaghetti-like forests are more difficult to measure, a misjudgment during the measurements could as well be the cause of this observation.

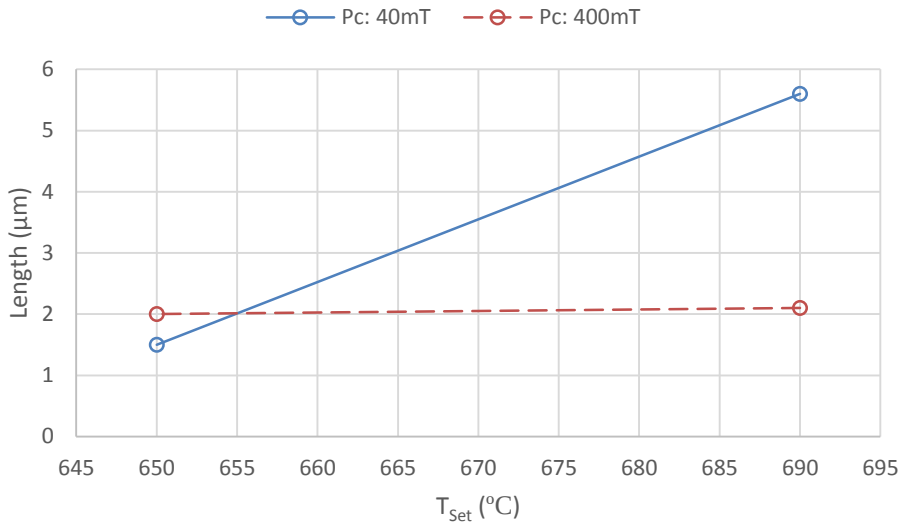

Graph 5.6: CNT length in relation to set temperature for the two partial pressure recipes at two different set temperatures.

N. Chiodarelli found that nanotubes resulting from 40 mTorr and 400 mTorr recipes at a total pressure of 4 Torr and a sample temperature of ~560°C (T_{Set}=650°C) are similar in length. This corresponds to the observations made here.

In general, it is believed that at low partial pressures the growth rate, and therefore the length, increases when the partial pressure is increased. This originated from the idea that at low partial pressures the kinetics are limited by the decomposition step. The growth rate is able to increase until the catalyst surface is saturated. At this point a leveling in CNT length would be expected since the concentration of the precursor on the catalyst surface would then become constant and independent of the partial pressure. However, in experiments like this one, a reduction of the CNT length is observed, which would suggest that the catalytic activity is reduced before saturation. This could be caused by two mechanisms. The first one could be the partial poisoning of active sites on the catalyst. A second one could be that adsorbed precursor molecules compete in such a way that they are suppressed before they can be absorbed by the catalyst. This could explain the length difference at 690°C.

5.7. Growth session 2: Pretreatment & total pressure

In general, it is believed that plasma pretreatments can assist the breakage of the nickel layer at lower temperatures. However, catalyst deactivation is a risk. Growth session 1 shows that NH_3 plasma works better than H_2 plasma. Therefore, it is interesting to explore whether a more gentle plasma treatment yields better results. In addition, it is determined whether a reduction of the total pressure at lower temperatures has a positive effect on the growth regarding the thermal pretreatment. The recipes and results of growth session 2 are shown in Table 5.4 and Table 5.5 respectively.

Note that the growth time is now set to 15 minutes instead of 10 minutes for session 1.

Table 5.4: Pretreatment and growth recipes for session 2.

02		Pretreatment							Carbon Deposition					
	Set ºC	Sccm	Sccm	Sccm	HF (W)	Torr	M'S''	Act ºC	Sccm	Sccm	Pressure		M' S''	Act ºC
Sample	Temp	H_2	NH_3	Ar	Plasma	Press	Time	Temp	C_2H_2	Ar	Tot(T)	Part(mT)	Time	Temp
01	690	200	-	600	-	1	5'	572	5	495	4	40	15'	613
02	690	-	100	-	50	1	2'30"	572	5	495	4	40	15'	613
03	650	200	-	600	-	1	5'	540	5	495	4	40	15'	579
04	650	-	100	-	50	1	2'30"	540	5	495	4	40	15'	579
05	600	200	-	600	-	1	5'	500	5	495	4	40	15'	535
06	600	-	-	-	-	-	-	-	5	495	4	40	15'	535
07	550	200	-	600	-	1	5'	460	5	495	4	40	15'	492
08	550	200	-	600	-	1	10'	460	5	495	4	40	15'	492
09	550	-	100	-	50	1	2'30"	460	5	495	4	40	15'	492
10	500	200	-	600	-	1	10'	420	5	495	4	40	15'	449

Table 5.5: Growth results of session 2.

Sample	Best/ Temp	Visual Quality	Comment	Alignment	Yield	$^{o}C_{set}$	Length µm	Diam. nm ±5
01	X	3	Curly bottom	straight	okay	690	2.3	13
02		2	Messy growth	curled	okay	690	1.5	16
03		2	Short/messy bottom	straight/ curled	okay	650	1.8	14
04	X	2	unbalanced growth	curled	okay	650	2.5	16
05		4	Bottom curly / Fat CNT top	curled	poor	600	1.5	12
06	X	4	Bottom curly / Fat CNT top	curled	okay	600	1.6	14
07	X	4	Bottom curly / Fat CNT top	curled	okay	550	1.6	18
08		4	Bottom curly / Fat CNT top	curled	okay	550	1.5	17
09		4	Curly bottom	curled	okay	550	1.1	19
10	X	4	Short tubes at bottom	curled	okay	500	1.2	15

Legend	
1 2 3 4	Alignment: packed > straight > curled > spaghetti > none Yield: good > okay > poor > none

5.7.1. Influence of temperature and plasma power on the NH_3 plasma pretreatment recipe

The goal of this comparison is to examine the evolution of the NH_3 plasma pretreatment at 50 W within a certain temperature range. These results will then be compared with the ones of the recipes conducted at 100 W (session 1) to find out which one yields better results. The qualitative part, based on SEM images, covers the NH_3 plasma recipes from session 2 (Table 5.4), while the quantitative part, based on length measurements, covers both the ones from sessions 1 at 100W (Table 5.2) and session 2 at 50W (Table 5.4).

Apart from the length, the forests at 690°C and 650°C remain very similar, while at a set temperature of 550°C, the forest structure completely changes (Figure 5.8). Even though it suffers from the smoke structure and yields the shortest tubes of the three, the forest turns out to be straighter and denser.

This result is promising since it seems that, despite some structural anomalies, an NH_3 plasma pretreatment works well at low temperatures.

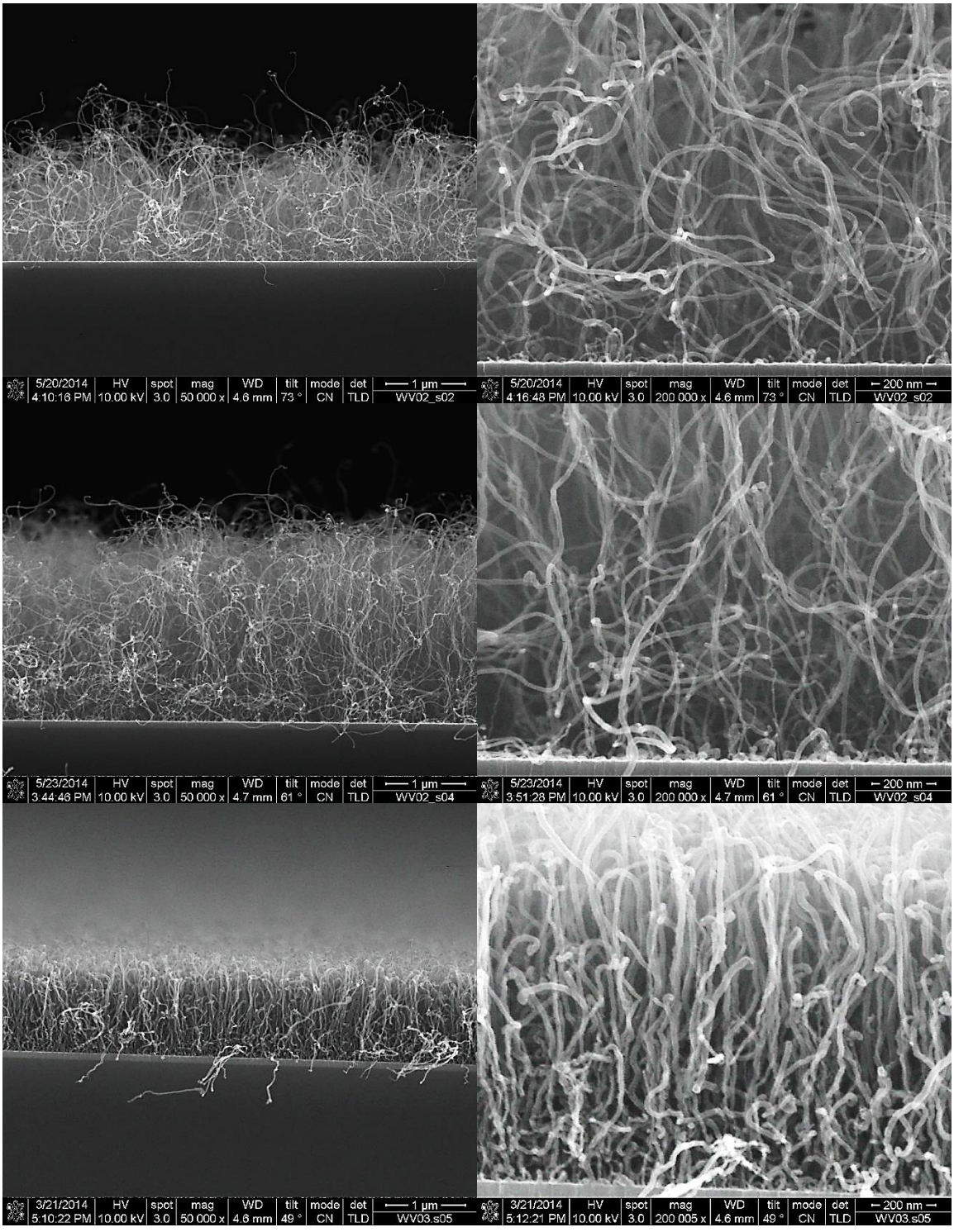

Figure 5.8: XSEM images of CNT growth with 50W NH_3 plasma pretreatment at three different set temperatures (Table 5.4) with (left) growth overview and (right) zoom in. Sample order from top to bottom: 02.02 690°C, 02.04 650°C, 02.09 550°C.

Plotting the CNT length towards the set temperature for the NH_3 plasma pretreatment recipes at both 50W and 100W, clearly shows that in general a higher plasma power delivers taller tubes (Graph 5.7). This feeds the idea that NH_3 plasma pretreatments are able to assist in breaking up the catalyst layer while still retaining sufficient catalytic activity. This idea is shared by N. Chiodarelli. However, more data is needed over a broader temperature and plasma power range in order to turn this idea into a statement.

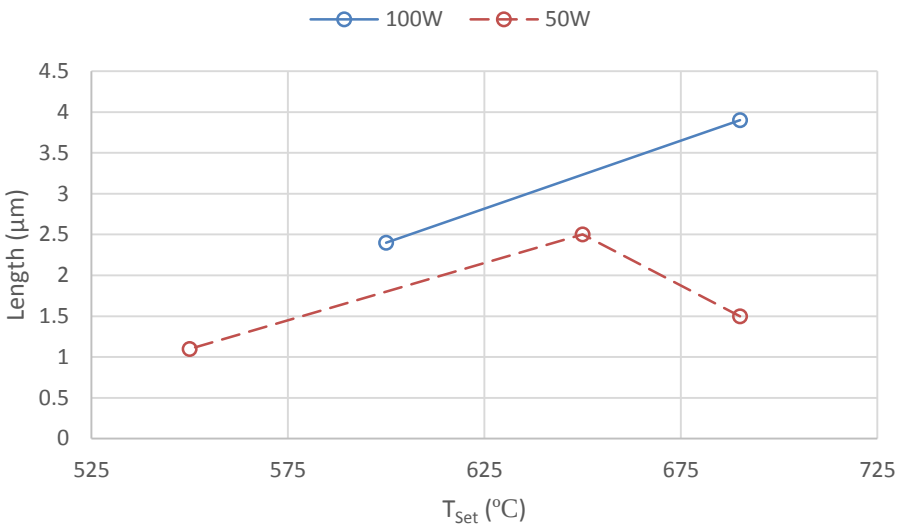

Graph 5.7: CNT length in relation to set temperature for the NH_3 plasma pretreatment recipes at 100W (blue) and 50W (red).

5.7.2. Influence of temperature on the thermal pretreatment recipe at lower total pressure

In this comparison, the evolution of the growth, resulting from the thermal pretreatment, is followed at a total pressure of 1 Torr over a certain temperature range. The goal of this experiment is to find out whether or not a lower total pressure yields better results at lower temperatures. The qualitative part covers the thermal recipes from session 2 (Table 5.4), while the quantitative part, based on length measurements, covers both the ones from sessions 1 at 4 Torr (Table 5.2) and session 2 at 1 Torr (Table 5.4).

It appears that although the CNT length declines together with declining temperature, the overall forest quality improves (Figure 5.9). The forest

density seems remarkably higher at 600°C and 550°C. However, this is accompanied by the presence of the typical smoke structure at lower temperatures. This increase in density results in a straighter alignment of the tubes. Based on the SEM images in Figure 5.9, it appears that a low total pressure enhances the growth at low temperatures, while a higher total pressure does the same at higher temperatures (Session 1).

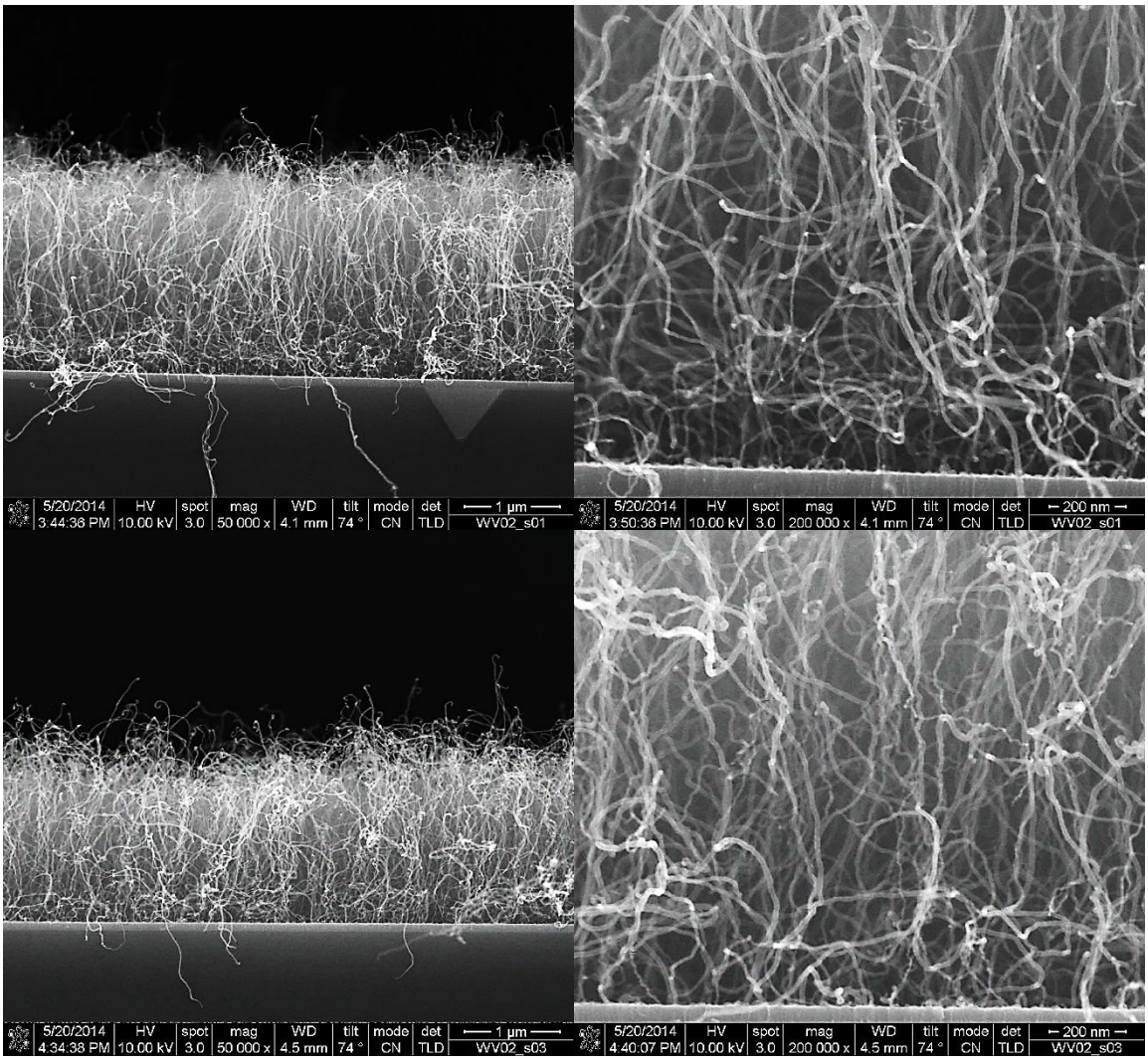

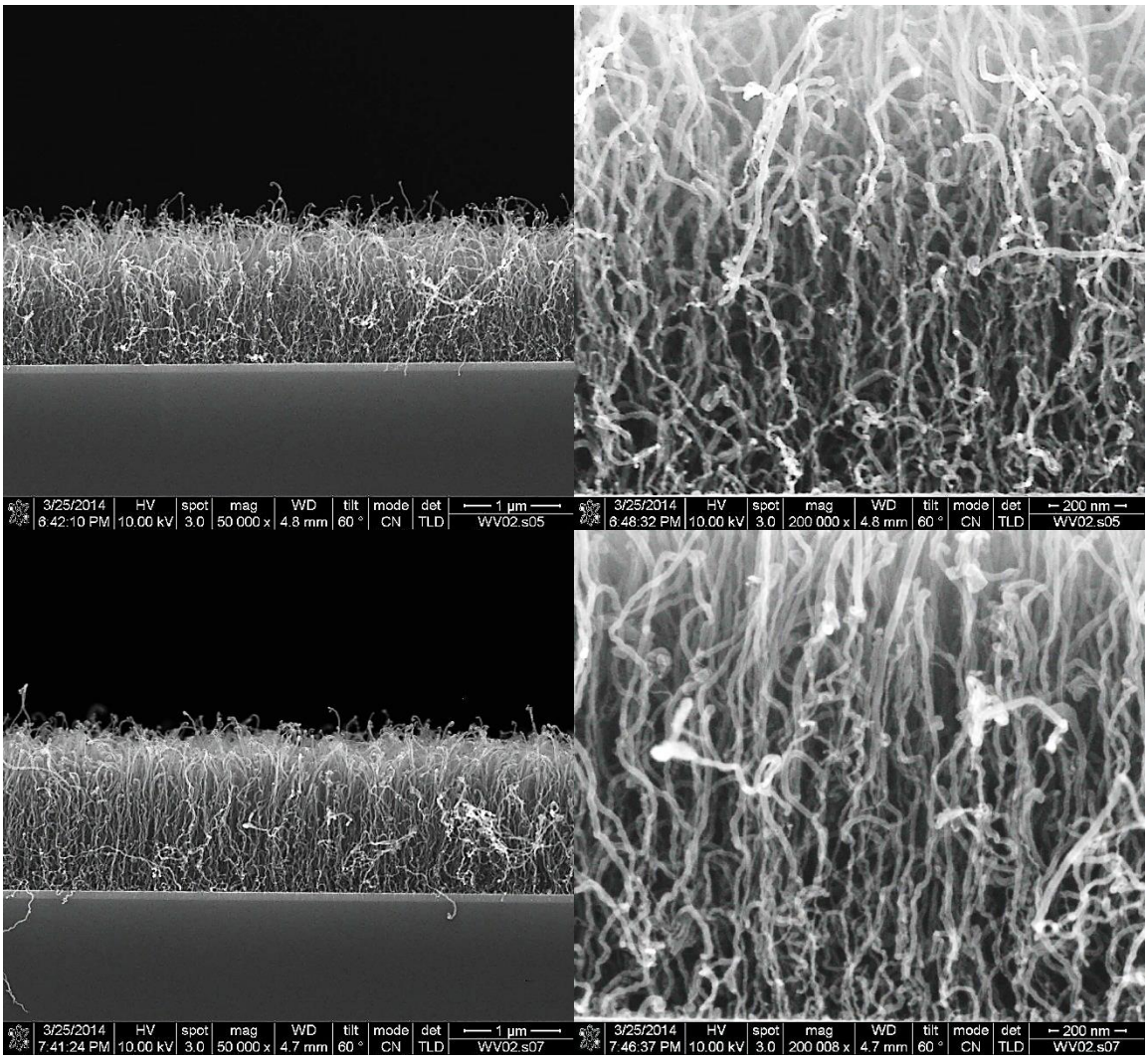

Figure 5.9: XSEM images of CNT growth with thermal pretreatment at total pressure of 1 Torr and different set temperatures (Table 5.4) with (left) growth overview and (right) zoom in. Sample order from top to bottom: 02.01 690°C, 02.03 650°C, 02.05 600°C, 02.07 550°C.

Plotting the CNT length towards the set temperatures sketches a slightly different picture. Based on CNT length alone, the 4 Torr recipe performs better in most cases, even at low temperatures (Graph 5.8). This is not surprising since a higher total pressure entails a better heat dispersion, thus a higher sample temperature. What is strange, however, is the decline in length towards higher temperatures. Also, the length at 690°C is out of proportion. In this respect, the evolution of the 1 Torr recipe is far more logical, yielding taller nanotubes at higher temperatures. In conclusion, the forest alignment and density get better towards lower temperatures for recipes at both 1 and 4 Torr, with a slight advantage for the 1 Torr recipe.

This could be due to a lower growth rate which leads to lesser structural defects. When it comes to length, the 4 Torr recipe seems to outperform the 1 Torr recipe in most cases.

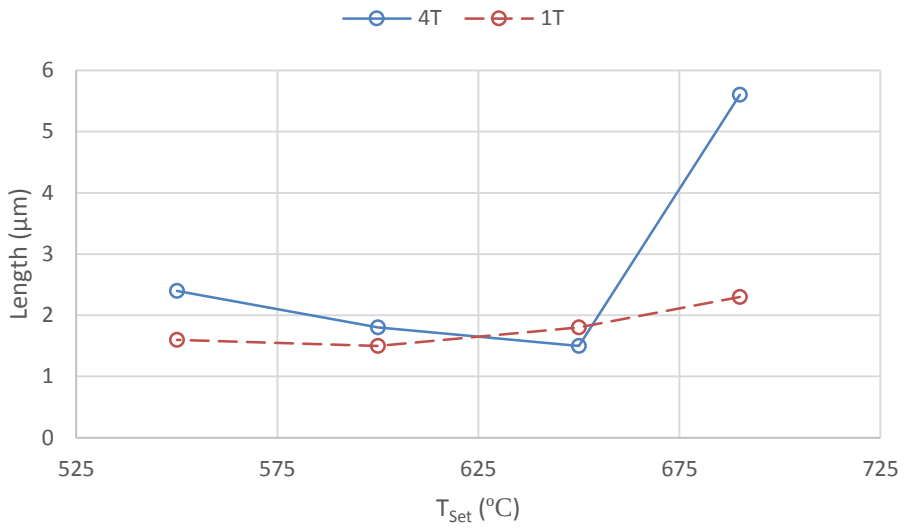

Graph 5.8: CNT length in relation to set temperature for the thermal pretreatment recipes at 4 Torr (blue) and 1 Torr (red).

In addition, the difference in pretreatment time between sample 07 and 08 does not seem to have any effect on both CNT length or diameter.

5.8. Growth session 3/4: Total and partial pressure

Growth sessions 3 and 4 focus mainly on varying the partial pressure of acetylene. In order to obtain various partial pressures, the total pressure and/or gas composition need to be modified, keeping in mind that they may also have an influence on the growth. Note that in this experiment the pretreatment step is omitted. Focusing on the experiments featuring the same set temperatures, three interesting comparisons can be made. First of all, the three recipes can be compared varying the partial pressures, which differ in order of magnitude of ten, namely 0.4 mTorr, 4.0 mTorr and 40 mTorr (Session 1, Sample 05, Table 5.2). Secondly, keeping the actual temperature constant. And last, using similar partial pressures at different

total pressures. All recipes and results of growth session 3 and 4 can be found in Table 5.6 and Table 5.7 respectively.

Unlike in previous tables, here the recipes are arranged according to increasing partial pressures in order to facilitate the comparisons. Because the total pressure varies significantly due to the design of the experiment, the actual temperature changes accordingly, so an actual temperature column is added to the results table.

The partial pressure is calculated as follows:

$$P_C = P_T * \left(\frac{F_C}{F_T}\right),$$

with

P_C = Partial pressure of the hydrocarbon precursor

P_T = Total pressure

F_C = Flow of the hydrocarbon precursor

F_T = Total flow

Table 5.6: Growth recipes for session 3/4.

3/4		Carbon Deposition							
	Set ºC	Sccm	Sccm	Sccm	Pressure		M' S"	Act ºC	Sccm
Sample	**Temp**	**C_2H_2**	**H_2**	**Ar**	**Tot(T)**	**Part(mT)**	**Time**	**Temp**	**He**
01	690	2	198	300	0.1	0.4	15'	567	6
02	690	2	198	300	0.4	1.6	15'	570	6
03	690	2	198	300	1	4.0	15'	572	6
04	690	1	198	500	4	5.7	15'	613	6
05	690	1	198	500	8	11.4	15'	630	10
06	690	2	200	495	4	11.5	15'	613	6
07	690	5	200	495	4	28.6	15'	613	6
08	750	5	-	495	4	40	15'	665	6
09	800	5	-	495	4	40	15'	708	6
10	800	5	-	495	8	80	15'	728	10

Table 5.7: Growth results of session 3/4.

Sample	Best/ Temp	Visual Quality	Comment	Alignment	Yield	°C$_{Set}$	°C$_{Act}$	Length µm	Diam. nm ±5
01		1	Barely any growth	spagh.	poor	690	567	0.12	19
02		3	Short tubes (Pc too low?)	straight	poor	690	570	0.6	13
03		3	Straight / short growth	straight	okay	690	572	1.3	16
04		4	Short tubes at bottom	straight	okay	690	613	2.1	16
05		4	Dense growth / clusters	straight	good	690	630	2.7	15
06		4	Dense growth / clusters	straight	good	690	613	3.4	24
07	X	4	Dense growth / clusters	straight	good	690	613	4.5	23
08	X	3	/	spagh./curled	poor	750	665	1.7	15
09		3	Length differences	spagh.	poor	800	708	1.3	14
10	X	4	/	spagh./curled	poor	800	728	2.1	15

Legend	
1 2 3 4	Alignment: packed > straight > curled > spaghetti > none Yield: good > okay > poor > none

5.8.1. Varying the partial pressure in order of magnitude of 10

Table 5.8: Recipes used in this comparison, where the partial pressure is varied in order of magnitude of 10.

		Carbon Deposition						
	Set °C	Sccm	Sccm	Sccm	Pressure		M' S"	Act °C
Sample	**Temp**	**C_2H_2**	**H_2**	**Ar**	**Tot(T)**	**Part(mT)**	**Time**	**Temp**
3/4.01	690	2	198	300	0.1	0.4	15'	567
3/4.03	690	2	198	300	1.0	4.0	15'	572
01.05	690	5	-	495	4.0	40.0	10'	613

Sample	Visual Quality	Comment	Alignment	Yield	Length µm	Diam. nm ±5
3/4.01	1	Barely any growth	spagh.	poor	0.1	19
3/4.03	3	Straight / short growth	straight	okay	1.3	16
01.05	4	Dense growth	straight	good	5.3	16

The recipes used in this comparison are shown above in Table 5.8.

Based on the SEM images, the evolution in CNT length is obvious. At 0.4 mTorr barely any growth is observed (Figure 5.10). This could be due to a carbon shortage at lower partial pressures, in combination with the lower actual temperature and total pressure, which cause low heat distribution. The alignment suffers from the poor growth because the nanotubes are not able to support each other during growth. In addition, the spaghetti-like structure could be caused by structural defects. The higher diameter could indicate the presence of CNFs. Aside from the length difference, the structure of the last two samples are very similar. They both feature a straight alignment where the nanotubes are fairly freestanding, while the diameter remains in the same range. This raises the question whether or not there exists a partial pressure minimum after which, aside from the length, the structure remains unchanged.

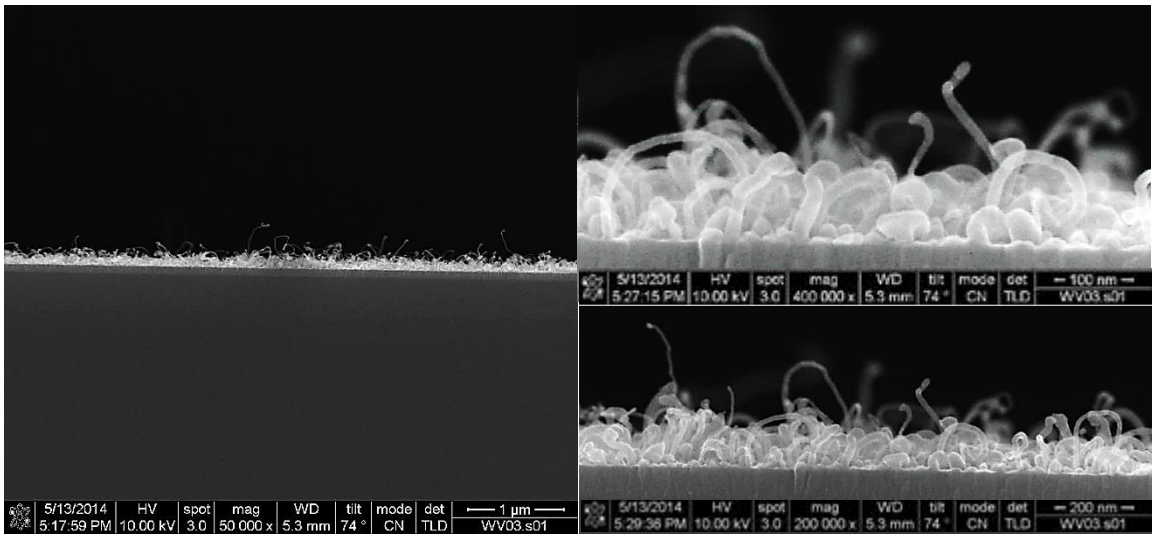

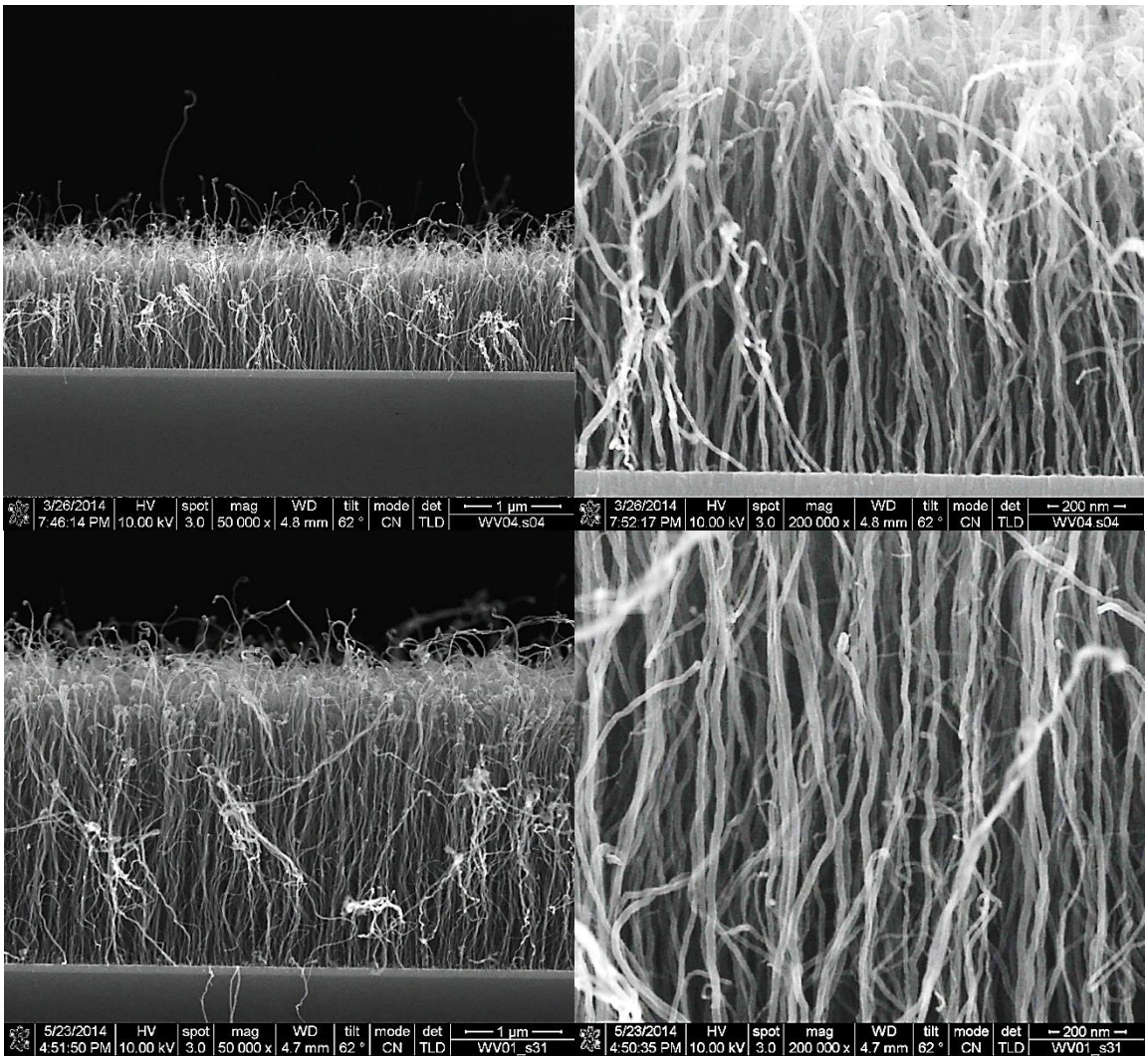

Figure 5.10: XSEM images of CNT growth with partial pressures of 0.4mT, 4.0mT and 40.0mT at a set temperature of 690°C (Table 5.8) with (left) growth overview and (right) zoom in. Sample order from top to bottom: 3/4.01 0.4mT, 3/4.03 4.0mT and 01.05 40.0mT.

Plotting the CNT length towards the partial pressure shows an increasing trend. Looking at the relation between the actual temperature and the partial pressure a similar trend is observed (Graph 5.9). This would imply there exists a correlation between the CNT length and the actual temperature, which would probably be due to a higher catalytic activity and kinetic energy at higher temperatures.

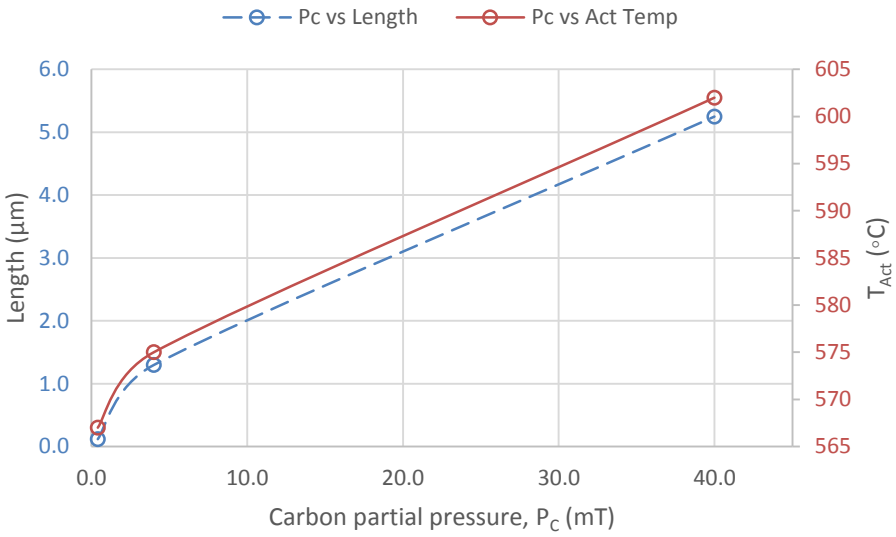

Graph 5.9: CNT length in function of partial pressure (blue), actual temperature in function of partial pressure (red).

However, alongside there not being enough data points to make a relevant conclusion, the total pressure plays a deceiving role. The relation between the actual temperature and the partial pressure is most likely due to the total pressure and not to the partial pressure itself, since they evolve in the same way. This is made clear in Graph 5.10 by substituting the partial pressure, with the total pressure.

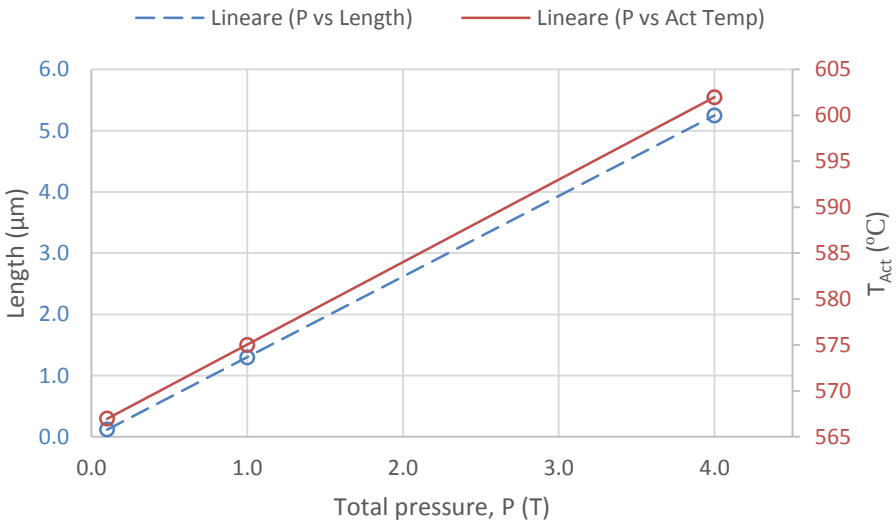

Graph 5.10: CNT length in function of total pressure (blue), actual temperature in function of total pressure (red).

This implies there exist a relation between the CNT length and the actual temperature, which is shown below in Graph 5.11.

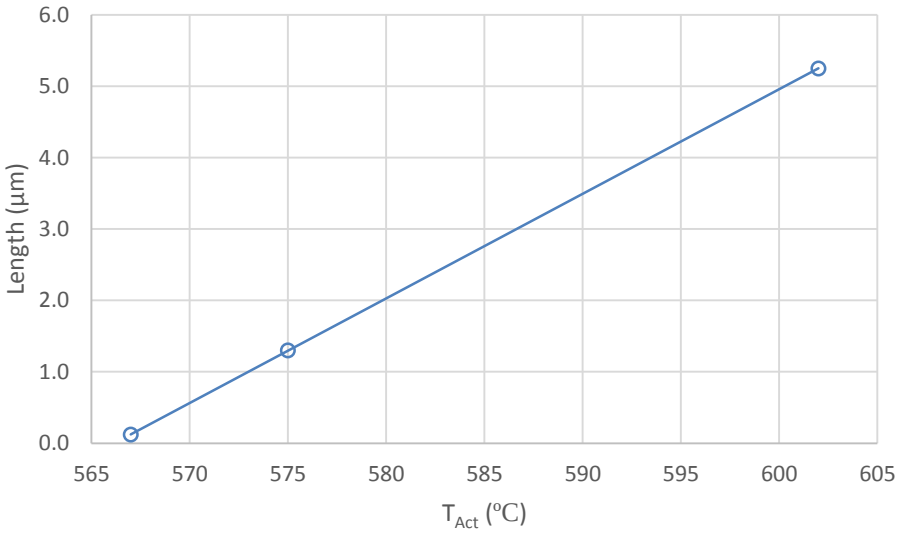

Graph 5.11: CNT length in relation to actual temperature.

However, the lack of data points in combination with the variations in total pressure and related actual temperature still prevent a conclusion concerning the relation between the CNT length and partial pressure. In order to be able to confirm this possible finding, new recipes have to be developed in which the total pressure is held constant. The next comparison is already a start in confirming this correlation.

5.8.2. Influence of the partial pressure at constant total pressure and actual temperature

As mentioned in the previous comparison, here we strive to keep the total pressure and related actual temperature constant. In order to do so, the gas composition is changed in such a way that changes concerning the gas ratio are kept to a minimum. The only exception to this logic is the last recipe, which is taken from the first growth session. Note that for this recipe the time-corrected length is used. The recipes for this comparison are shown below in Table 5.9.

Table 5.9: Recipes used to examine the influence of the partial pressure at constant total pressure and temperature.

		Carbon Deposition						
	Set °C	Sccm	Sccm	Sccm	Pressure		M' S"	Act °C
Sample	**Temp**	**C_2H_2**	**H_2**	**Ar**	**Tot(T)**	**Part(mT)**	**Time**	**Temp**
3/4.04	690	1	198	500	4	5.7	15'	613
3/4.06	690	2	200	495	4	11.5	15'	613
3/4.07	690	5	200	495	4	28.6	15'	613
01.05	690	5	-	495	4	40.0	10'	613

Sample	Visual Quality	Comment	Alignment	Yield	Length µm	Diam. nm ±5
3/4.04	**4**	Short tubes at bottom	straight	okay	2.1	16
3/4.06	**4**	Dense growth / clusters	straight	good	3.4	24
3/4.07	**4**	Dense growth / clusters	straight	good	4.5	23
01.05	**4**	Dense growth	straight	good	5.3	16

Judging from the SEM images (Figure 5.11), the length difference between the first sample and the others is striking. In addition, when looking at the more detailed view, the first sample shows short, immature nanotubes at the bottom of the forest. Similar tubes, although lower in numbers, are also present on the second sample whereas on the last sample they are completely absent. This raises the question whether the addition of hydrogen gas plays a role in this phenomenon or if lowering the total pressure at lower partial pressures could resolve this (see sample 3/4.03). Further, it can be noticed that, especially in sample two and three, the CNTs tend to form bundles, whereas on the last samples they are more freestanding. Moving on to the orientation of the forest, all samples feature a straight alignment with an upwards orientation. The orientation of sample three deviates a bit by leaning to one side. This is probably due to the age and the handling of the sample at the moment of undergoing SEM. Last, the diameter distribution appears to be similar for every sample.

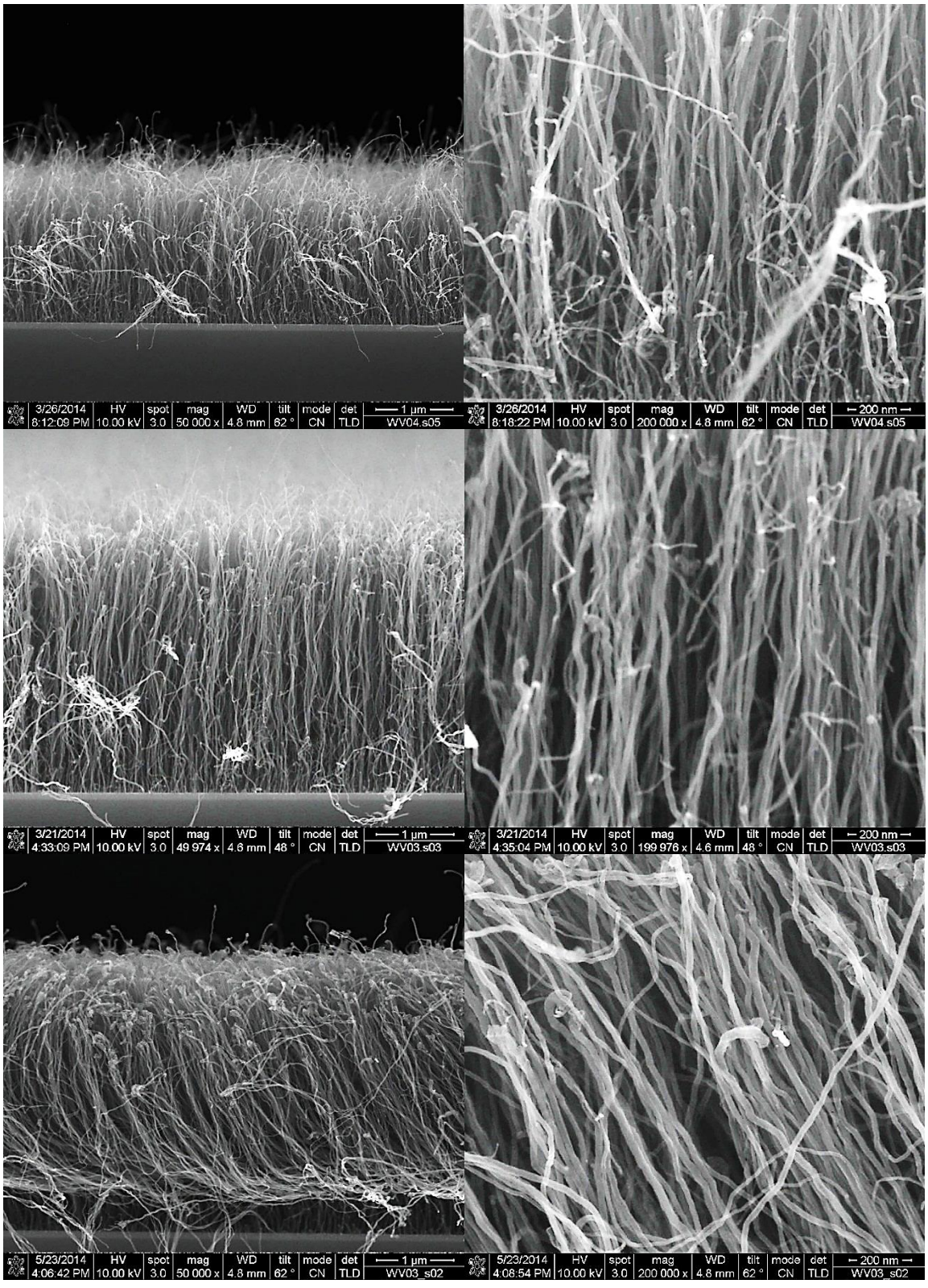
3/26/2014 8:12:09 PM | HV 10.00 kV | spot 3.0 | mag 50 000 x | WD 4.8 mm | tilt 62 ° | mode CN | det TLD | 1 µm | WV04.s05
3/26/2014 8:18:22 PM | HV 10.00 kV | spot 3.0 | mag 200 000 x | WD 4.8 mm | tilt 62 ° | mode CN | det TLD | 200 nm | WV04.s05
3/21/2014 4:33:09 PM | HV 10.00 kV | spot 3.0 | mag 49 974 x | WD 4.6 mm | tilt 48 ° | mode CN | det TLD | 1 µm | WV03.s03
3/21/2014 4:35:04 PM | HV 10.00 kV | spot 3.0 | mag 199 976 x | WD 4.6 mm | tilt 48 ° | mode CN | det TLD | 200 nm | WV03.s03
5/23/2014 4:06:42 PM | HV 10.00 kV | spot 3.0 | mag 50 000 x | WD 4.8 mm | tilt 62 ° | mode CN | det TLD | 1 µm | WV03_s02
5/23/2014 4:08:54 PM | HV 10.00 kV | spot 3.0 | mag 200 000 x | WD 4.8 mm | tilt 62 ° | mode CN | det TLD | 200 nm | WV03_s02

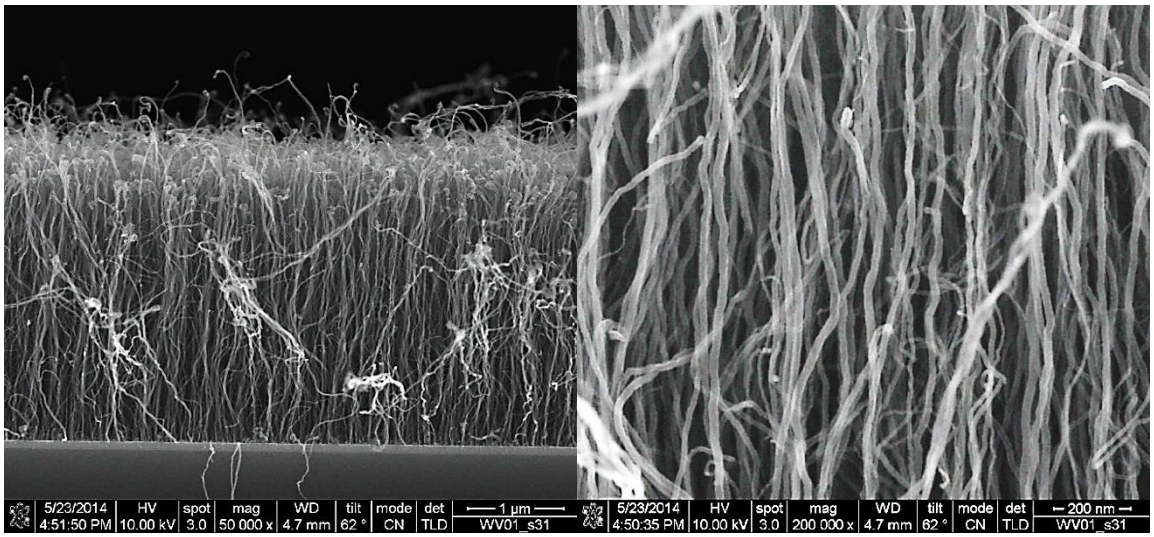

Figure 5.11: XSEM images of CNT growth with varying partial pressures at constant total pressure and related actual temperature (Table 5.9) with (left) growth overview and (right) zoom in. Sample order from top to bottom: 3/4.04 5.7mT, 3/4.06 11.5mT, 3/4.07 28.6mT and 01.05 40.0mT.

Plotting the CNT length towards the partial pressure confirms the trend that was shown before (Graph 5.12). A possible reason for this could be that at higher partial pressures more carbon is available. This ensures that the catalyst particle reaches his supersaturated state faster, whereby the growth process is initiated earlier. In other words, at higher partial pressure the crystallization step starts earlier and therefore lasts longer.

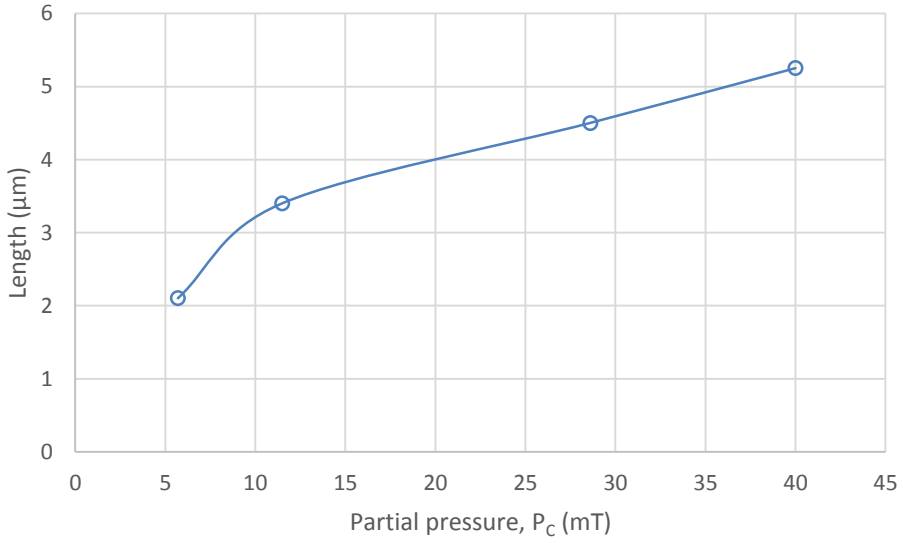

Graph 5.12: CNT length in relation to the partial pressure with constant total pressure and temperature.

A similar relation was found by N. Chiodarelli, using cobalt as a catalyst. More experiments, over a wider partial pressure range, should be performed.

5.8.3. Influence of the total pressure at similar partial pressures and temperatures

Earlier, a correlation between the CNT length and total pressure was reported up to 4 Torr. However, when looking at recipes with similar partial pressures at different total pressures a decline in length is observed at 8 Torr. Two groups of two recipes are studied, which feature quasi-constant partial pressures within their group. Each group features one recipe at 4 Torr, with the second one being at 1 or 8 Torr. The described recipes are shown in Table 5.10.

Table 5.10: Recipes used to examine the influence of the total pressure at similar partial pressures and temperatures.

		Carbon Deposition						
	Set ºC	Sccm	Sccm	Sccm	Pressure		M' S"	Act ºC
Sample	**Temp**	**C_2H_2**	**H_2**	**Ar**	**Tot(T)**	**Part(mT)**	**Time**	**Temp**
3/4.03	690	2	198	300	1	4.0	15'	572
3/4.04	690	1	198	500	4	5.7	15'	613
3/4.05	690	1	198	500	8	11.4	15'	630
3/4.06	690	2	200	495	4	11.5	15'	613

Sample	Visual Quality	Comment	Alignment	Yield	Length µm	Diam. nm ±5
3/4.03	**3**	Straight / short growth	straight	okay	1.3	16
3/4.04	**4**	Short tubes at bottom	straight	okay	2.1	16
3/4.05	**4**	Dense growth / clusters	straight	good	2.7	15
3/4.06	**4**	Dense growth / clusters	straight	good	3.4	24

At first, the structures that result from the first two recipes at ~5 mT seem very alike, featuring straight, freestanding tubes (Figure 5.12). However, as cited before, the forest grown at 4 Torr suffers from short, immature tubes at the bottom. This feeds the idea that the total pressure could be responsible for this phenomenon at low partial pressures. Although, the possible

influence of H_2 gas cannot be ruled out since the difference in argon flow leads to a shift in H_2 partial pressure. The length difference is easily explained by the difference in total pressure and related actual temperature.

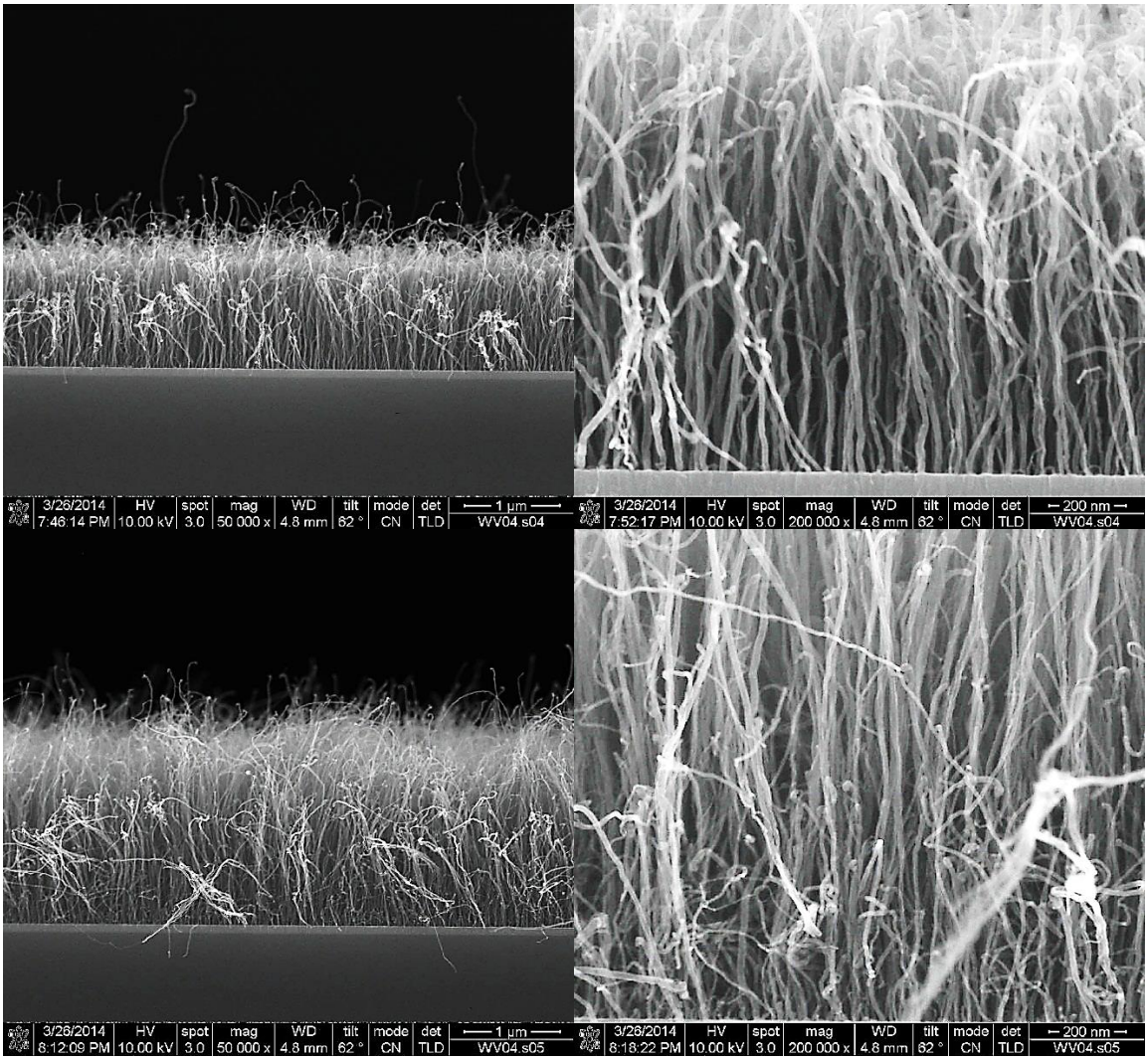

Figure 5.12: XSEM images of CNT growth with two total pressure recipes at quasi constant partial pressure of ~5mT (Table 5.10) with (left) growth overview and (right) zoom in. Sample order from top to bottom: 3/4.03 1T and 3/4.04 4T.

Both samples grown at a partial pressure of ~11.5 mTorr feature dense growth with the occasional formation of clusters (Figure 5.13). Although, the actual temperature and heat distribution are greater at 8 Torr, the CNT length, surprisingly, is not. The absence of short, immature tubes at 4 Torr and their presence at 8 Torr might suggest that a balance between the total and partial pressure is needed to avoid these immature tubes. The

remarkable difference in CNT diameter is moderately noticeable judging from the SEM images at larger magnification. The high figure could be coincidence due to an unfortunate choice in used CNTs during measurements.

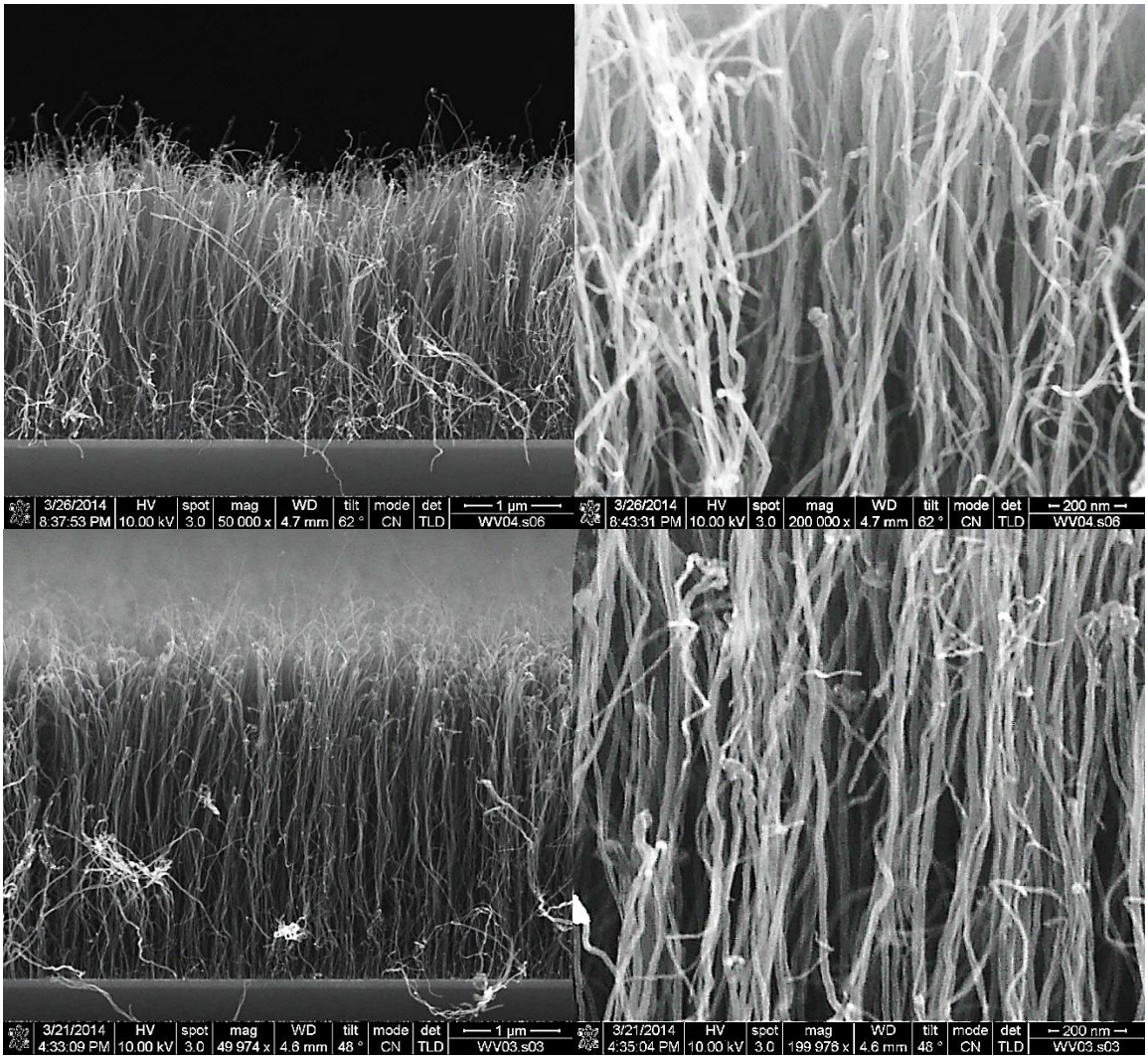

Figure 5.13: XSEM images of CNT growth with two total pressure recipes at quasi constant partial pressure of ~11.5mT (Table 5.10) with (left) growth overview and (right) zoom in. Sample order from top to bottom: 3/4.05 8T and 3/4.06 4T.

Plotting the CNT length towards the partial pressure for these four recipes, a tilt in CNT length is observed concerning the total pressure. Despite the few data, there seems to exist a total pressure optimum in these conditions. Judging from Graph 5.13, the optimum is to be expected somewhere between 1 Torr and 8 Torr. The rationale for this pressure optimum could be that at lower total pressures the amount of precursor gas reaching the

catalyst is inadequate, whereas when the total pressure is too high catalyst poisoning occurs in an earlier stage. However, although the differences in partial pressure within the same group are negligible, it is not always the case for the actual temperature and gas composition. To address these design flaws, a new set of recipes is developed.

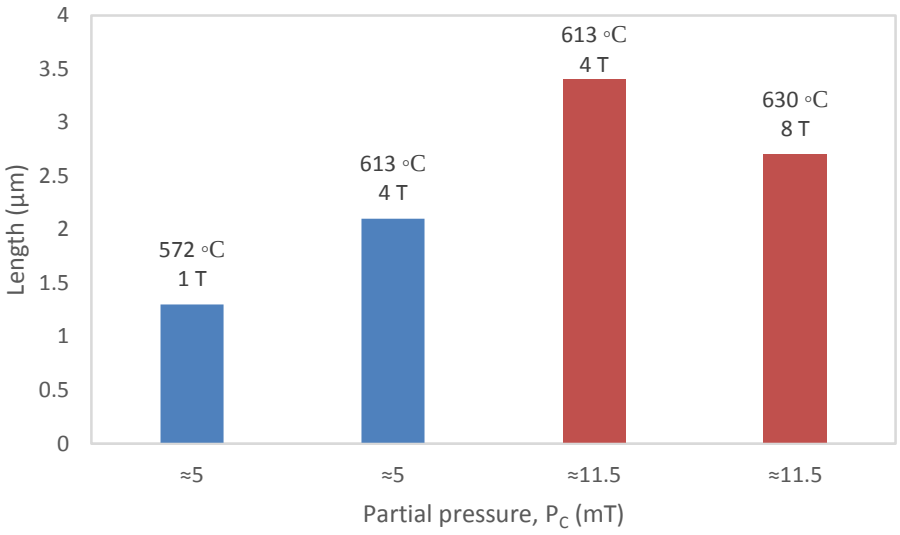

Graph 5.13: CNT length in relation to partial pressure in which the length of two groups of two recipes are compared in relation to the total pressure.

In order to confirm this possible finding, a new set of recipes is designed where the partial pressure is kept constant over several total pressures. To ensure the actual temperature remains constant as well, the set temperature is adapted in function of the total pressure. In order to match the parameters to one another, only the gas composition is changed in such a way that the total and sub flows do not deviate too much from each other, while keeping the restrictions of the tool in mind.

In addition, the recipes can be performed at two set temperature ranges, above and below 690°C. The reason behind this is that while the runtime for CNT growth is faster below 690°C, the actual temperature in this case might be too low to yield decent growth at all total pressures. Therefore it would be wise to perform the experiment at both temperatures to ensure the reliability of the results. The discussed recipes can be found in Table 5.11.

Table 5.11: Future recipes concerning the confirmation of a decline in CNT length at high total pressures at constant partial pressures and actual temperatures.

		Carbon Deposition							
	Set ºC	Sccm	Sccm	Sccm	Pressure		M' S"	Act ºC	Sccm
Sample	**Temp**	**C_2H_2**	**H_2**	**Ar**	**Tot(T)**	**Part(mT)**	**Time**	**Temp**	**He**
01 / 09	690 / 774	8	152	240	1	20	15'	572 / 639	6
02 / 10	673 / 755	4	156	240	2	20	15'	573 / 639	6
03 / 11	642 / 720	2	158	240	4	20	15'	574 / 639	6
04 / 12	625 / 700	1	159	240	8	20	15'	575 / 639	10
05 / 13	690 / 774	16	144	240	1	40	15'	576 / 639	6
06 / 14	673 / 755	8	152	240	2	40	15'	577 / 639	6
07 / 15	642 / 720	4	156	240	4	40	15'	578 / 639	6
08 / 16	625 / 700	2	158	240	8	40	15'	579 / 639	10

These recipes are not performed yet due to technical problems with the PECVD tool. If it appears that these partial pressure groups show the same trend, additional total pressures can be used to enhance the data resolution. In addition, more recipes can be designed for 5 mTorr and 10 mTorr.

5.9. Clean and cooldown

After each growth session a clean and cooldown procedure is performed. First the process chamber is cooled down to below 270ºC, followed by a clean procedure involving O_2 plasma. The O_2 plasma oxidizes possible carbon residues to CO_2, which are then removed out of the chamber. Lastly, a second cooldown period brings the chamber down to room temperature. The whole process takes about one hour.

Conclusion

The research field of carbon nanotubes is challenging. The amount of parameters that play a role in the growth process is so extensive that despite a research time of over 20 years and heaps of publications, uncertainty about the growth mechanism is still high and more advanced applications have yet to see the light of day. However, despite the few data, this thesis is able to make a small contribution within the more narrow field of CNT interconnects. Regarding the pretreatment step, it was found that there is no superior pretreatment type for all temperatures. In addition, NH_3 plasma appears to be more gentle to the catalyst than H_2 plasma at relatively high temperatures and is thus able to preserve the catalytic activity better. Moreover, a higher plasma power appears to result in taller forests. Furthermore, it appears that a temperature optimum can be found for a specific growth recipe and that forest quality and length can differ significantly with temperature. In addition, it was found that at low partial pressures, CNT length increases with increasing partial pressure, whereas at high partial pressures the situation is reversed. Lastly, it appears that a total pressure optimum exists for recipes at quasi constant partial pressures. However, let it be clear that most of what is found here can only be considered as signs of possible correlations and that it would be premature to draw any definitive conclusions from these few data. An idea for future research could be to add oxygen-containing gases to the gas mixture, as literature indicates that this could enhance the growth significantly. Since only oxygen itself is available on the used PECVD tool, this experiment was not yet conducted for safety reasons. Looking to the future, there is still a lot of work ahead in order to reach the goal of implementation in 2020. To date, it is doubtful whether this deadline will be met. However, the world of carbon nanotubes remains fascinating and will keep challenging the minds of people for many years to come. [6][52][53]

Bibliography

[1] F. Cain, "What is a Space Elevator?". In: *Universe Today*. **2013**. URL: http://www.universetoday.com/105441/what-is-a-space-elevator

[2] W. Bacsa. "Who discovered carbon nanotubes? - All you need to know about the discovery of carbon nanotubes". In: *Scitizen*. **2006**.

[3] M. Monthioux. "Who should be given the credit for the discovery of carbon nanotubes?". In: *Carbon*. **2006**, 44, 1621.

[4] M. Kumar, Y. Ando. "Chemical Vapor Deposition of Carbon Nanotubes: A Review on Growth Mechanism and Mass Production". In: *Journal of Nanoscience and Nanotechnology*. **2010**, 10, 3739-3758.

[5] "Audacious and Outrageous: Space Elevators". In: *Nasa Science*. **2000**. URL: http://science1.nasa.gov/science-news/science-at-nasa/2000/ast07sep_1/

[6] M. Kumar. "Carbon Nanotube Synthesis and Growth Mechanism". In: *Carbon Nanotubes: Synthesis, Characterization, Applications*. **2011**.

[7] D. Gualtieri. "Transparent and Conductive". **2011**. URL: http://tikalon.com/blog/blog.php?article=2011/ITO

[8] J. Sloan. "The Key to CNTs: Functionalization". In: High-Performance Composites. **2010**. URL: http://www.compositesworld.com/articles/the-key-to-cnts-functionalization

[9] J. P. Gore, A. Sane. "Flame Synthesis of Carbon Nanotubes". In: *Carbon Nanotubes: Synthesis, Characterization, Applications*. **2011**.

[10] "Carbon nanotube". In: *Wikipedia*. URL: http://en.wikipedia.org/wiki/Carbon_nanotube

[11] R. Prada Silvy, Y. Tan, P. Wallis. "Single-walled Carbon Nanotubes: Recent Advances, Manufacturing, Characterization and Applications". In: *CoMoCAT Carbon Nanotubes*. URL: http://www.sigmaaldrich.com/materials-science/nanomaterials/comocat-carbon-nanotubes.html#top

[12] K. E. Nordheim. "Growth and Properties of Carbon Nanotubes". **2012**.

[13] M. Yu, B. I. Yakobson, R. S. Ruoff. "Controlling Sliding and Pullout of Nested Shells in Individual Multiwalled Carbon Nanotubes". In: *J. Phys. Chem. B*. **2000**, 104, 8764-8767.

[14] G. Eres. "Carbon Nanotubes". URL: http://www.asdn.net/asdn/chemistry/carbon_nanotubes.shtml

[15] T. A. Adams II. "Physical Properties of Carbon Nanotubes". **2000**. URL: http://www.pa.msu.edu/cmp/csc/ntproperties/

[16] D. Dass, R. Prasher, R. Vaid. "Single Walled CNT Chirality Dependence for Electrical Device Applications". In: *The African Review of Physics*. **2013**, 8, 0005.

[17] N. Chiodarelli. "Correlation between number of walls and diameter in multiwall carbon nanotubes grown by chemical vapor deposition". In: *Carbon*. **2012**, 50, 1748-1752.

[18] N. Dunne, W. Ornsby. "MWCNT Used in Orthopaedic Bone Cements". In: *Carbon Nanotubes: Growth and Applications*. **2011**.

[19] M. van der Veen. "Carbon Nanotubes". In: *Imec Training*. **2012**.

[20] D. A. Martin. "Trends in Nanotubes Research." **2006**.

[21] S. Mori, M. Suzuki. "Non-Catalytic, Low-Temperature Synthesis of Carbon Nanofibers bt Plasma-Enhanced Chemical Vapor Deposition". In: *Nanofibers*. **2010**.

[22] "A Comparison of Carbon Nanotubes and Carbon Nanofibers". **2011**. URL: http://pyrografproducts.com/carbon-nanotubes.html

[23] I. Martin-Gullon, J. Vera, J. A. Conesa, J. L. Gonzalez, C. Merino. "Differences between carbon nanofibers produced using Fe and Ni catalysts in a floating catalyst reactor". In: *Carbon*. **2006**, 44, 1572-1580.

[24] G. Lee, S. Han, J. Yu, J. Ihm. "Catalytic decomposition of acetylene on Fe(001): A first-principles study". In: *Physical Review B*. **2002**, 66, 081403.

[25] C. Journet, M. Picher, V. Jourdain. "Carbon nanotube synthesis: from large-scale production to atom-by-atom growth". In: *Nanotechnology*. **2012**, 23, 142001.

[26] P. Serp, J. L. Figueiredo. "Carbon Materials for Catalysis". **2009**.

[27] J. Tessonnier, D. S. Su. "Recent Progress on the Growth Mechanism of Carbon Nanotubes: A Review". In: *ChemSusChem*. **2001**, 4, 824-847.

[28] F. Ding. "The Limits of Carbon Nanotube (CNT) Growth". URL: http://159.226.49.43/download/ICT-HPCC12/July_9/Feng_Ding.pdf

[29] S. Hofmann, G. Csanyi, A. C. Ferrari, M. C. Payne, J. Robertson. "Surface Diffusion: The Low Activation Energy Path for Nanotube Growth". In: *Physical Review Letters*. **2005**, 95, 036101.

[30] C. T. Wirth, S. Hoffmann, J. Robertson. "State of the catalyst during carbon nanotube growth". In: *Diamond and Related Materials*. **2009**, 18, 940-945.

[31] "Ostwald ripening". In: *Wikipedia*. URL: http://en.wikipedia.org/wiki/Ostwald_ripening

[32] "Ostwald Ripening". URL: http://pssnicomp.com/definitions/ostwald-ripening/

[33] "Tutorial 6: Ostwald Ripening". URL: http://xray.bmc.uu.se/~terese/crystallization/tutorials/tutorial6.html

[34] J. A. Kpetsu, P. Jedrzejowski, C. Coté. "Influence of Ni Catalyst Layer and TiN Diffusion Barrier on Carbon Nanotube Growth Rate". In: *Nanoscale Res Letters*. **2010**, 5, 539-544.

[35] N. Chiodarelli. "Carbon Nanotubes as Future Interconnects for sub-32nm Technologies". **2011**.

[36] A. Gohier, C. P. Ewels, T. M. Minea, M. A. Djouadi. "Carbon nanotube growth mechanism switches from tip- to base- growth with decreasing catalyst particle size". In: *Carbon*. **2008**, 46, 1331-1338.

[37] I. K. Song, Y. S. Cho, G. S. Choi, J. B. Park, D. J. Kim. "The growth mode change in carbon nanotube synthesis in plasma-enhanced chemical vapor deposition". In: *Diamond and Related Materials*. **2004**, 13, 1210-1213.

[38] L. Delzeit, I. McAninch, B. A. Cruden, D. Hash, B. Chen, J. Han, M. Meyyappan. "Growth of multiwall carbon nanotubes in an inductively coupled plasma reactor". In: *Journal of Applied Physics*. **2002**, 91, 6027.

[39] "Chemical Vapor Deposition". URL: https://sites.google.com/site/nanomodern/Home/CNT/syncnt/cvd

[40] J. Park. "Chemical Vapor Deposition". **2001**.

[41] J. Schmidt, M. Kerr, A. Cuevas. "Surface passivation of silicon solar cells using plasma-enhanced chemical-vapour-deposited SiN films and thin thermal SiO_2/plasma SiN stacks". In: *Semiconductor Science and Technology*. **2000**, 16, 164.

[42] "PECVD". URL: http://www.plasmatherm.com/pecvd.html

[43] "What is PECVD?". URL: http://www.plasmaequip.com/WHAT%20IS%20PECVD.pdf

[44] S. R. Shamsudin. "Scanning electron microscope (SEM) and how it works". **2011**. URL: http://emicroscope.blogspot.be/2011/03/scanning-electron-microscope-sem-how-it.html

[45] "Scanning Electron Microscopy (SEM)". URL: http://www.gla.ac.uk/schools/ges/research/researchfacilities/isaac/services/scanningelectronmicroscopy/

[46] "SEM Illustrative Example: Secondary Electron and Backscatter Electron Images". URL: http://www.andersonmaterials.com/sem/sem-secondary-backscatter-images.html

[47] S. Swapp. "Scanning Electron Microscopy (SEM)". URL: http://serc.carleton.edu/research_education/geochemsheets/techniques/SEM.html

[48] "Scanning Electron Microscopy". URL: http://www.nanoscience.com/products/sem/technology-overview/

[49] "Scanning Electron Microscopy – Advantages and Disadvantages in Imaging Components and Applications". URL: http://www.microscopemaster.com/scanning-electron-microscope.html

[50] "Auger effect". In: *Wikipedia*. URL: http://en.wikipedia.org/wiki/Auger_effect

[51] M. Golabadi, R. Ajeian, M. Nakhaiebadrabadi. "Study of Temperature effect on Synthesis of Carbon Nanotubes by Iron Catalyst and Ethanol vapor by Chemical Vapor Deposition (CVD)". In: *Proceeding of the 4th International Conference on Nanostructures*. **2012**.

[52] W. Shi. "The Role of Oxygen in Carbon Nanotube Synthesis". **2014**.

[53] S. Arkalgud. "Interconnect Opportunities – A SEMATECH Perspective". **2012**.